




# Ecosystem changes through the Permian–Triassic and Triassic–Jurassic critical intervals: Evidence from sedimentology, palaeontology and geochemistry

YU PEI\*†‡ , MARTIN BLUMENBERG‡, JAN-PETER DUDA\*†§, NILS HÖCHE¶ ,  
JÖRN PECKMANN\*\* , DANIEL BIRGEL\*\*, JINXIONG LUO††, KURT KMENT‡‡ and  
JOACHIM REITNER†§

\*Department of Geosciences, Eberhard Karls Universität Tübingen, Schnarrenbergstrasse 94-96, Tübingen, 72076, Germany (E-mail: [yu.pei@mnf.uni-tuebingen.de](mailto:yu.pei@mnf.uni-tuebingen.de))

†‘Origin of Life’ Group, Göttingen Academy of Sciences and Humanities, Theater Strasse 7, Göttingen, 37073, Germany (E-mail: [jreitne@gwdg.de](mailto:jreitne@gwdg.de))

‡Federal Institute for Geosciences and Natural Resources, Stilleweg 2, Hannover, 30655, Germany

§Department of Geobiology, Geoscience Center, Georg-August-Universität Göttingen, Goldschmidtstrasse 3, Göttingen, 37077, Germany

¶Institute for Geosciences, Johannes Gutenberg Universität Mainz, Johann-Joachim-Becher-Weg 21, Mainz, 55118, Germany

\*\*Institute for Geology, Center for Earth System Research and Sustainability, Universität Hamburg, Bundesstrasse 55, Hamburg, 20146, Germany

††School of Geosciences, Yangtze University, College Road 111, Wuhan, 430100, China

‡‡In der Vogelau 20, Teisendorf, 83317, Germany

Associate Editor – Nathan Sheldon

## ABSTRACT

The Permian–Triassic and Triassic–Jurassic critical intervals are among the most significant ecological upheavals in the Phanerozoic. Both evolutionary junctures are characterized by environmental deterioration associated with a marked biodiversity decline. In this study, Permian–Triassic and Triassic–Jurassic boundary sections from South China and the Northern Calcareous Alps were investigated. In order to reconstruct the interplay between biotic and abiotic processes, a multifaceted approach that included optical microscopy, X-ray diffraction, Raman spectroscopy, stable carbon isotopes and lipid biomarkers was employed. The lower parts of these two sections are similar as both consist of limestone with abundant fossils of eukaryotic organisms. However, the Permian–Triassic record is dominated by dasyclad green algae and fusulinid foraminifera, while the Triassic–Jurassic record is typified by corals and coralline sponges. Moving upward, both sections consist mainly of micrite and marl. Concerning the Permian–Triassic section, it transits to volcanic ash intercalated by a distinct limestone bed with abundant calcispheres (tentatively attributed to ancestors of dinoflagellates). The Triassic–Jurassic section does not provide direct evidence for volcanic activity, but also becomes rich in calcisphere-type cysts towards the top. Additionally, the section preserves abundant 4-methyl sterenes (diagnostic for dinoflagellates) and C<sub>37–39</sub> n-alkanes (indicative for haptophytes). Hence, both critical intervals were associated with marked blooms of (ancestral) dinoflagellates and haptophytes (for example, coccolithophorids). These blooms were followed by ecological lag-phases, as indicated by low carbonate contents and scarce fossils which only increased further up the sections. For both critical intervals, it is commonly assumed that the formation of voluminous volcanic provinces (Siberian Traps and Central Atlantic Magmatic Province, respectively), as well as associated

processes (for example, burning of organic-rich sediments such as coal), resulted in ecological devastation. However, results suggest that volcanism also had a positive effect on certain planktonic primary producers such as dinoflagellates and haptophytes, perhaps by delivering essential nutrients.

**Keywords** Calcispheres, dinoflagellates, haptophytes, lipid biomarkers, mass extinctions, microfacies, stable carbon isotopes.

## INTRODUCTION

Most Phanerozoic extinction events are identified by quantitative analyses using databases of marine fossil organisms (e.g. Raup, 1979; Sepkoski *et al.*, 1981; Raup & Sepkoski, 1982; Bambach, 2006; Alroy *et al.*, 2008; Fan *et al.*, 2020). Two of the most severe Phanerozoic mass extinctions coincide with ecological upheavals during the Permian–Triassic (P–T) and Triassic–Jurassic (T–J) critical intervals. Both events have been intimately associated with the formation of large continental flood basalt provinces: the Siberian Traps and the Central Atlantic Magmatic Province (CAMP), respectively (Whiteside *et al.*, 2010; Blackburn *et al.*, 2013; Burgess & Bowring, 2015; van de Schootbrugge & Wignall, 2016; Burgess *et al.*, 2017; Davies *et al.*, 2017; Broadley *et al.*, 2018). In addition to the relative timing of the events, the potential relationship between volcanism and ecosystem change is evidenced by widespread occurrences of volcanic ash layers and mercury anomalies in marine sedimentary rocks (Thibodeau *et al.*, 2016; Percival *et al.*, 2017; Wang *et al.*, 2018).

Geochemical evidence encoded in sedimentary rocks contributes to the understanding of ecological upheavals during the P–T and T–J intervals. For instance, significant shifts in the stable carbon isotopic composition of P–T carbonates are proposed to reflect significant perturbances in the global carbon cycle at that time (Payne *et al.*, 2004). Similarly, profound shifts in the stable sulphur isotopic composition of sulphate and carbonate-associated sulphate might indicate that the global biogeochemical sulphur cycle was affected as well (Luo *et al.*, 2010; Song *et al.*, 2014; Bernasconi *et al.*, 2017). During the T–J crisis, major biogeochemical cycles were also strongly perturbed as reflected by significant carbon and sulphur isotopic fluctuations (Williford *et al.*, 2009; Ruhl *et al.*, 2010, 2011; Ruhl & Kürschner, 2011).

During the P–T and T–J crises, many parts of the oceans perhaps became oxygen-poor or even anoxic, also in the photic zone (Brennecke *et al.*, 2011; Richoz *et al.*, 2012; Jaraula *et al.*, 2013;

Blumenberg *et al.*, 2016; Huang *et al.*, 2017; Zhang *et al.*, 2018), and seawater pH decreased (Payne *et al.*, 2010; Greene *et al.*, 2012; Hinojosa *et al.*, 2012; Clarkson *et al.*, 2015). However, one major difference between the two critical intervals might have been seawater temperatures: P–T oceans were suggested to be lethally hot (up to 36°C) based on the  $\delta^{18}\text{O}_{\text{apatite}}$  conodont record (Joachimski *et al.*, 2012; Sun *et al.*, 2012), perhaps driving the expansion of anoxic conditions (Penn *et al.*, 2018), whilst T–J oceans are characterized by mild to warm temperatures (*ca* 13 to 30°C) as indicated by clumped-isotope palaeothermometry studies on microbialites (Petryshyn *et al.*, 2020). During the P–T crisis, hypercapnia (i.e. abnormally high CO<sub>2</sub> levels in the blood of organisms, causing physiological problems) might have also driven ecosystem change (Knoll *et al.*, 2007), which is supported by high atmospheric carbon dioxide contents (Wu *et al.*, 2021).

This study tracks ecosystem changes through the P–T and T–J critical intervals in South China and the Northern Calcareous Alps, respectively. Following a geobiological approach, the study combined techniques from sedimentology, palaeontology and biogeochemistry, including optical microscopy, X-ray diffraction, Raman spectroscopy, stable carbon isotopes and lipid biomarkers. The detailed comparison of records from both localities allows identification of fundamental similarities and differences between the P–T and T–J events, which is of great significance to the ongoing discussion of possible causes and triggers of mass extinctions.

## GEOLOGICAL SETTINGS

### South China

South China is a key area for investigating the P–T critical interval because of the abundance of easily accessible outcrops and sections comprising well-preserved strata. This study focuses on the Xiakou section (N 31°06.874', E 110°48.209'), close to Xiakou town, Hubei Province (Fig. 1A).

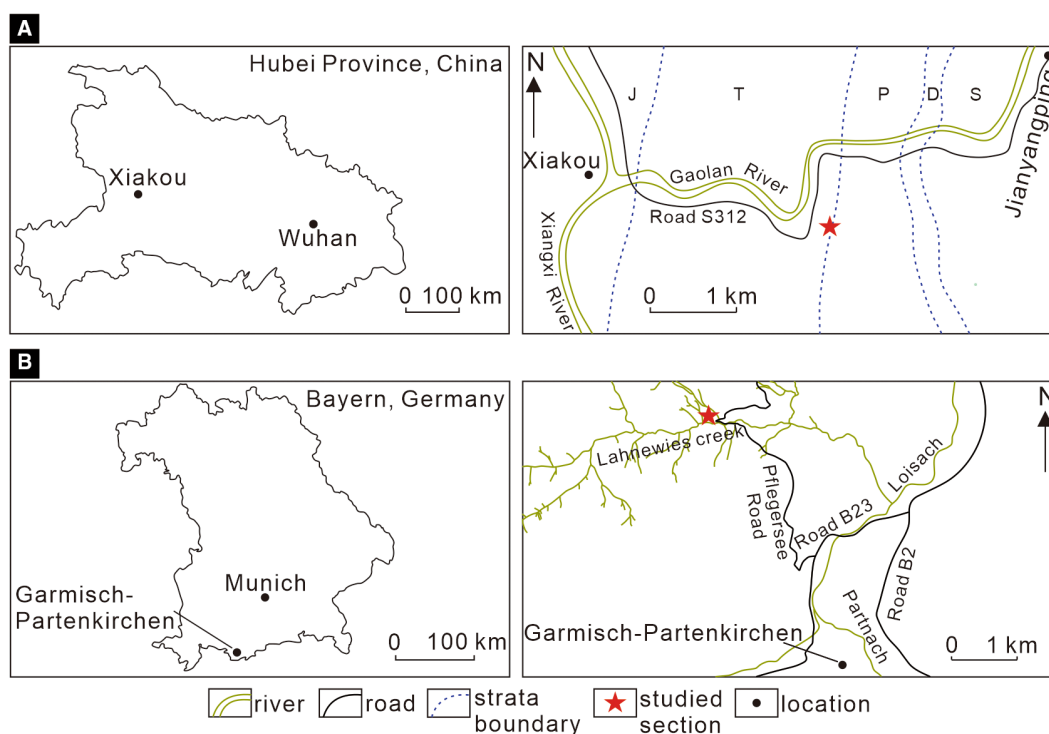


**Fig. 1.** (A) Location of the Permian–Triassic (P–T) Xiakou section (modified from Pei *et al.*, 2021), between the town of Xiakou and the village of Jianyangping (Hubei province, South China). The strata were indicated after Luo *et al.* (2009). (B) Location of the Triassic–Jurassic (T–J) Lahnewies Syncline section, the main part exposed close to the Lahnewies creek near Garmisch-Partenkirchen, Southern Germany. J, Jurassic; T, Triassic; P, Permian; D, Devonian; S, Silurian.

In this area, a marine transgression at the end of the Permian resulted in a transition from shallow open platform (Changhsingian, Late Permian) to deeper shelf basin environments (Induan, Early Triassic) (Fig. 1A; Feng *et al.*, 1997; Luo *et al.*, 2009). Stratigraphically, the Xiakou section comprises the Changxing and Dalong formations (Changhsingian, Upper Permian) as well as the Daye Formation (terminal Changhsingian, Upper Permian to Induan, Lower Triassic). The lowest occurrence of the conodont *Hindeodus parvus* at the base of bed T<sub>1</sub> in the Daye Formation marks the beginning of the Triassic (Fig. 2; Zhao *et al.*, 2013). The base of bed T<sub>1</sub> can thus be correlated with the base of bed 27c of Meishan Section D (Changxing County, Zhejiang Province, China), the Global Stratotype Section and Point (GSSP) of the P–T boundary (Yin *et al.*, 2001; Zhang *et al.*, 2009). The Meishan record comprises palaeontological evidence for two mass extinction episodes (ME 1 and ME 2) across the P–T boundary (Song *et al.*, 2013), which are correspondingly identified in the Xiakou section (Fig. 2; Pei *et al.*, 2021).

### Northern calcareous Alps

During the T–J critical interval, the area of today's Northern Calcareous Alps was situated at the margin of the Meliata Ocean, which was part of the Neotethys (Stampfli & Borel, 2002). It is a key region for studying the T–J boundary because sedimentary successions represent a variety of different palaeoenvironments (e.g. Fabricius, 1966; Kuss, 1983; Mandl, 2000; McRoberts *et al.*, 2012). The Lahnewies Syncline, located in the Ammer Mountains near Garmisch-Partenkirchen, Bavaria, belongs to the northern part of the upper Austroalpine Lechtal nappe and is traversed by various longitudinal and transverse faults (Kuhnert, 1967; Karl *et al.*, 2014; Hornung & Haas, 2017). The stratigraphic section investigated herein is composed of two parts that are both situated in the western limb of the Lahnewies Syncline. More precisely, the main part is exposed close to the Lahnewies Creek (N 47°31.578', E 11°04.002') (Fig. 1B), while the second part is exposed in the Nudelgraben Creek (N 47°29.045', E 10°56.542'). The T–J Lahnewies Syncline section shares many

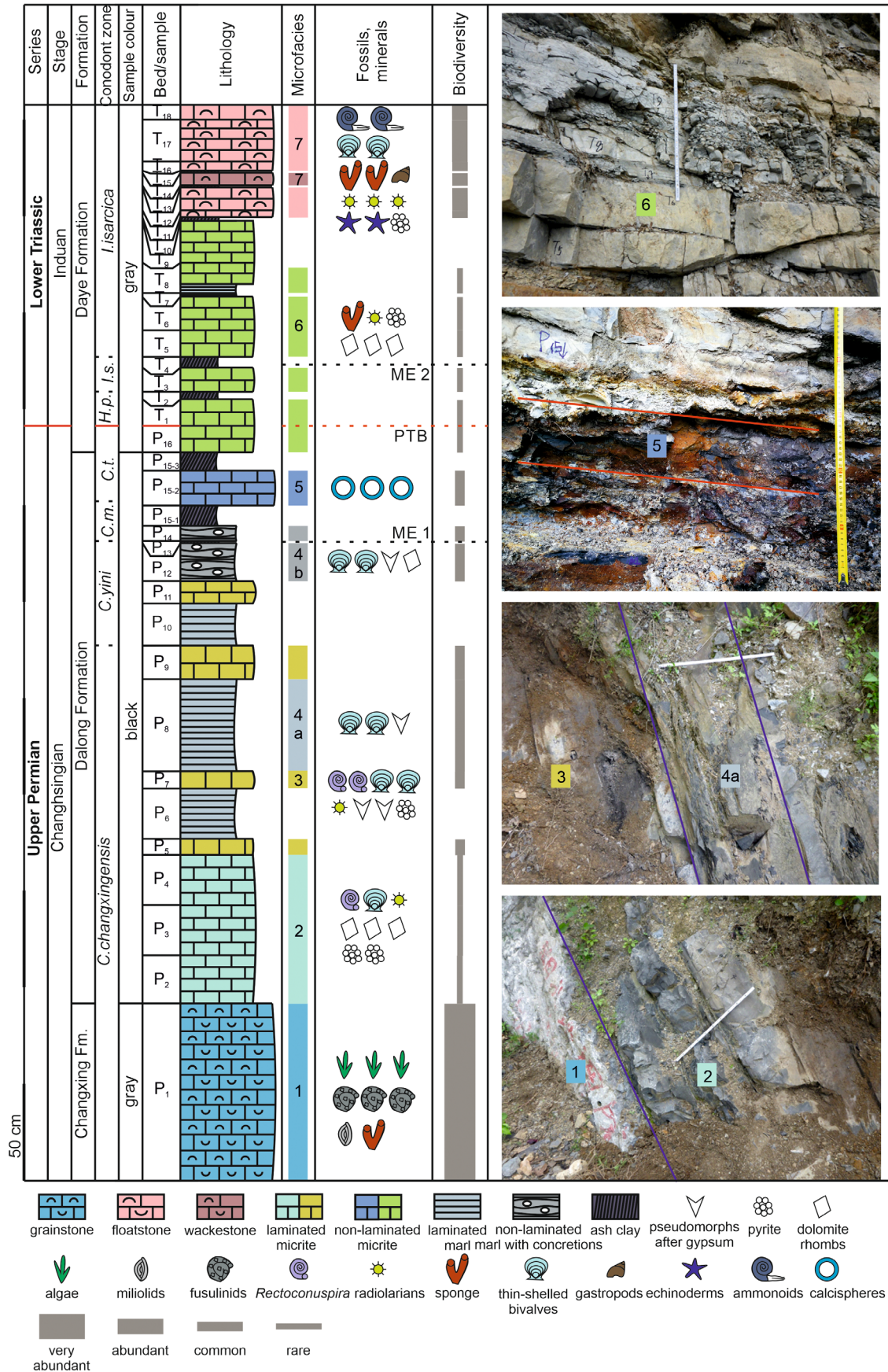


**Fig. 2.** The Xiakou section, displaying the lithology, microfacies, fossils and minerals, biodiversity and field photographs (modified from Pei *et al.*, 2021). ME 1, Mass extinction 1 (after Song *et al.*, 2013); PTB, Permian–Triassic boundary (after Zhao *et al.*, 2013); ME 2, Mass extinction 2 (after Song *et al.*, 2013); *C.m.*, *Clarkina meishanensis*; *C.t.*, *Clarkina taylorae*; *H.p.*, *Hindeodus parvus*; *I.s.*, *Isarcicella staeschei*. White ruler = 50 cm. Yellow ruler = 50 cm.

similarities with the GSSP section at Kuhjoch in the Karwendel-Syncline (Hillebrandt *et al.*, 2007, 2013).

Detailed descriptions on the stratigraphy of the Upper Triassic in the Northern Calcareous Alps have been provided elsewhere (Fig. 3; Mandl, 2000; Krystyn *et al.*, 2005; McRoberts *et al.*, 2012; Karl *et al.*, 2014). Briefly, sections across the T–J boundary typically begin with dolomites of the Hauptdolomit Formation (middle to upper Norian, Upper Triassic), which represented inter-supratidal environments on the Dachstein carbonate platform. The Norian–Rhaetian Dachstein Formation also includes ‘Ober-rhaetkalk’ of the Kössen Basin and Sevatian Plattenkalk unit as a shallow subtidal facies between supratidal to subtidal back-reef facies of the Dachstein Reef complex. The Hauptdolomit Formation is locally overlain by limestones of the Plattenkalk unit (Sevatian/upper Norian, Upper Triassic), which formed in slightly deeper, shallow subtidal environments on the platform. Both facies develop into the Kössen Formation (Rhaetian, Upper Triassic), which represents an open marine lagoonal back reef environment – the bathymetrically deepest part of the Dachstein carbonate platform. To the

south, the Dachstein carbonate platform was bordered by deep water environments of the Hallstatt Basin, which was part of the Meliata Ocean. These environments are represented by fore reef marls of the Zlambach Formation, which is equivalent to the lagoonal Kössen Formation (Fig. 3; Fabricius, 1966).

The Kössen Formation can be subdivided into the Hochalm and Eiberg members. The Eiberg Member is terminated by *ca* 50 to 100 cm thick T-Bed, which is strongly enriched in organic matter at its top. The T-Bed is of crucial stratigraphic significance because it can be traced throughout the area and contains terminal Triassic index fossils such as the ammonite *Choristoceras marshi* and the conodont *Misikella posthersteini* (e.g. Kozur & Mock, 1991; Krystyn, 2008).

The Eiberg Member is overlain by the Tiefengraben Member (Kendelbach Formation, terminal Triassic to lowermost Jurassic) characterized by carbonate-poor mudstones (for example, Schattwald Bed). The stratigraphic boundary within the Tiefengraben Member is indicated by occurrences of the ammonite *Psiloceras spelae*, which is a marker for the Hettangian (Hillebrandt & Krystyn, 2009). In the study area, the Tiefengraben Member is followed by deeper marine deposits of

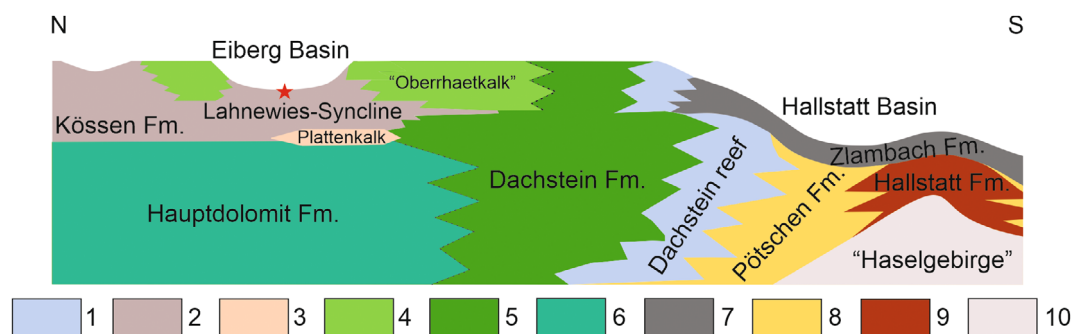


**Fig. 3.** Lithostratigraphic chart of the Upper Triassic in the Northern Calcareous Alps. The Lahnewies Syncline section was located within the Eiberg Basin (Mandl, 2000; Krystyn *et al.*, 2005; McRoberts *et al.*, 2012; Karl *et al.*, 2014). 1 = Dachstein reef facies of corals and sponges; 2 = open marine lagoonal Kössen facies; 3 = Plattenkalk; 4 = ‘Ober-rhaetkalk’; 5 = Dachstein back reef inter-supratidal loferite facies; 6 = Hauptdolomit facies representing distal back reef supra-intertidal facies; 7 = Rhaetian Zlambach fore reef facies; 8 = Norian Pötschen deep water fore reef facies; 9 = Norian Hallstatt facies of reddish pelagic deep-water carbonates; 10 = Late Permian evaporitic sequences (‘Haselgebirge’).

the Breitenberg Member (Kendelbach Formation; upper Hettangian, Lower Jurassic) and the Scheibelberg Formation (upper Hettangian to Sinemurian) (Figs 3 and 4; Hillebrandt et al., 2013). The stratigraphic age of the Scheibelberg Formation is indicated by ammonites such as

*Angulaticeras* cf. *marmoreum* and *Vermiceras* sp. (Kment, 2000). The Scheibelberg Formation is dominated by spiculitic limestones with chert nodules characterized by abundant bioturbation, representing a mid-shelf environment (Figs 3 and 4; Kuhnert, 1967; Böhm, 2003; Karl et al., 2014).

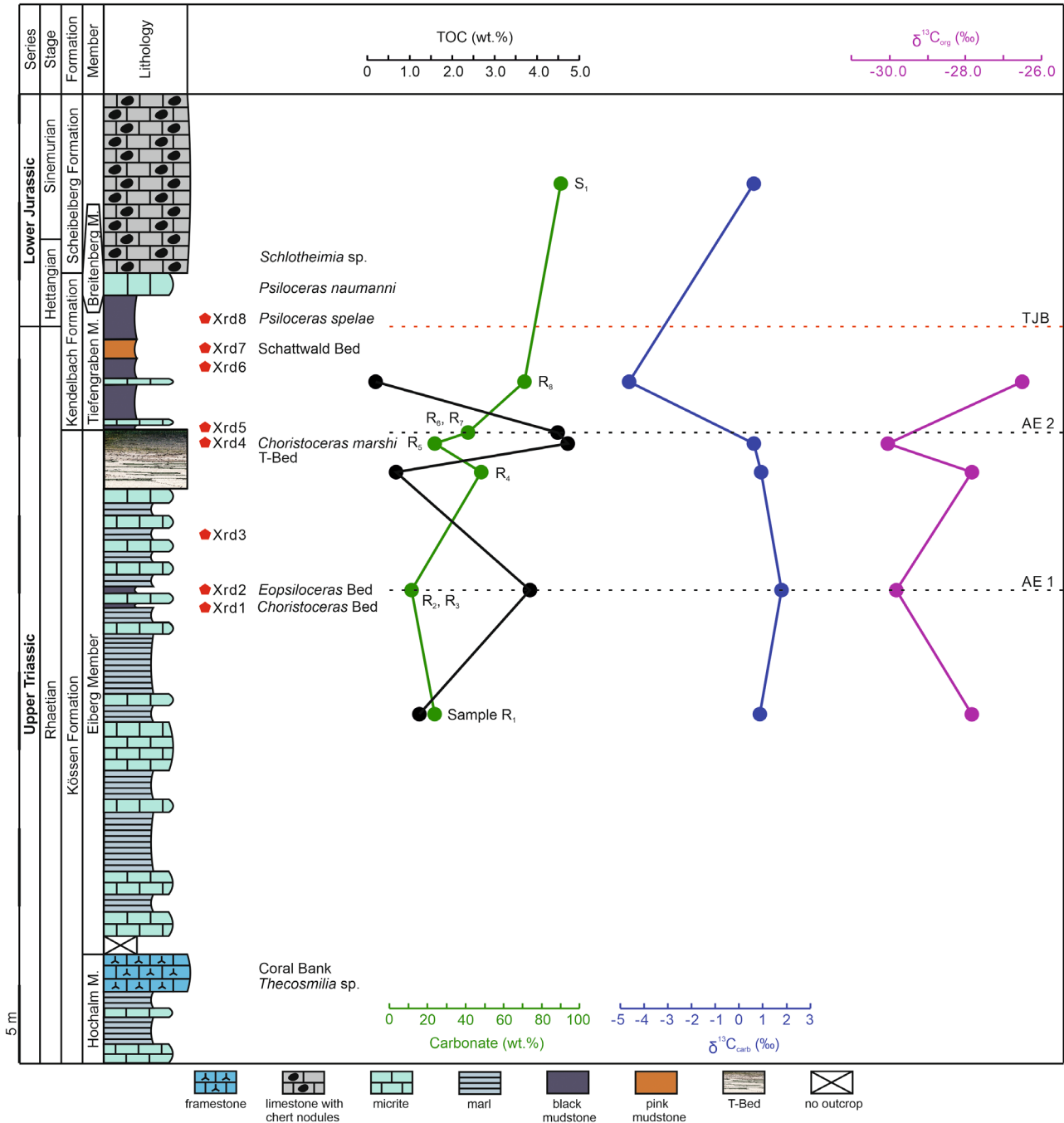


**Fig. 4.** The Lahnewies Syncline section, reconstructed from various tectonically displaced parts. Displayed together with profiles of bulk geochemical data, including carbonate (wt.%), TOC (wt.%) and profiles of stable isotopic data, including  $\delta^{13}C_{carb}$  (‰) and  $\delta^{13}C_{org}$  (‰). Eight samples from X-ray diffraction (Xrd1–8) are also displayed. AE 1, Anoxic Event 1; AE 2, Anoxic Event 2; TJB, Triassic–Jurassic boundary.

## MATERIALS AND METHODS

### Fieldwork and petrography

Field work in South China and the Northern Calcareous Alps has been conducted over several years and included careful observation of geological, sedimentological and palaeontological features as well as sampling. This was particularly important in the case of the Lahnewies Syncline, as sections and stratigraphic units are commonly tectonically separated. Details about the Xiakou section can be found in Pei *et al.* (2021).

Thin sections and smear slides were prepared for the analysis of microfacies and nannoplankton-type fossils (for more details on the latter see Janofske, 1987). Microfacies analysis was performed with a Zeiss SteREO Discovery.V12 stereomicroscope and a Zeiss AXIO Imager. Z1 microscope (Carl Zeiss AG, Jena, Germany). For fluorescence microscopy, the Zeiss AXIO Imager. Z1 microscope was equipped with a 10 AF488 filter (excitation wavelength = BP 450 to 490 nm, emission wavelength = BP 515 to 565 nm). Cathodoluminescence microscopy was conducted with a Zeiss Axiolab microscope combined with a Citl CCL 8200 Mk3A cold-cathode system (operating voltage of *ca* 15 kV; electric current of *ca* 250 to 300  $\mu$ A) (Cambridge Image Technology Limited, Hatfield, UK). For field emission scanning electron microscopy (FE-SEM), a Carl Zeiss LEO 1530 Gemini system was used.

Raman spectroscopy was performed with a WITec alpha300 R fibre-coupled ultra-high throughput spectrometer (532 nm excitation laser, operated at 20 mW, 100 $\times$  long working distance objective with numerical aperture of 0.75 and a 300 g mm<sup>-1</sup> grating) (Oxford Instruments Plc, Abingdon, UK). Centred at 2220 cm<sup>-1</sup>, the spectrometer covered a spectral range from 68 to 3914 cm<sup>-1</sup> with a spectral resolution of 2.2 cm<sup>-1</sup>. Each spectrum was collected by two accumulations, with an acquisition time of 2 s. The Raman spectra were analysed via the WITec Project software. Automated cosmic ray correction, background subtraction and fitting using a Lorentz function were performed.

### Bulk analyses

X-ray diffraction analysis (XRD) was conducted with a Philips PW 1800 (step size = 0.02 $^\circ$ , 2 $\theta$  = 3 to 70 $^\circ$ ; 4 s per step) and an Orion Komet P2 (step size = 0.02 $^\circ$ , 2 $\theta$  = 4 to 70 $^\circ$ ; 8 s per step)

(XRD Eigenmann GmbH, Schnaittach-Hormersdorf, Germany).

Total organic carbon (TOC) and total inorganic carbon (TIC) contents were measured with a Leco RC612, a Leco CS230 (Leco Corporation, St. Joseph, MI, USA) and an Euro EA 3000 elemental analyser (HEKAtech GmbH, Wegberg, Germany). All values are reported in weight % (wt.%) of bulk sedimentary rock. TOC and TIC contents of P–T samples were partially published in Pei *et al.* (2021).

Programmed pyrolysis of the P–T samples was carried out at Applied Petroleum Technology (Oslo, Norway), using a HAWK instrument (Wildcat Technologies, Humble, Texas, USA). The Late Triassic samples were run at the Federal Institute for Geosciences and Natural Resources (BGR) in Hannover, Germany, on a Rock-Eval-6 analyser (Vinci Technologies, Nanterre, France). Following established protocols (Espitalié *et al.*, 1977; Lafargue *et al.*, 1998), the temperature was ramped from 300 $^\circ$ C (held for 3 min) to 650 $^\circ$ C at 25 $^\circ$ C min<sup>-1</sup>. Initial sample weights were between 10 mg and 200 mg, depending on the expected hydrocarbon yields from labile kerogen (S2, see below) to prevent oversaturation of the flame ionization detector (FID). The analyses included quantities of free hydrocarbons (S1, mg HC g<sup>-1</sup> rock), S2 (mg HC g<sup>-1</sup> rock), temperatures at maximum yields of S2 hydrocarbons ( $T_{\max}$ ,  $^\circ$ C), and the CO<sub>2</sub> generated from organic carbon at higher temperatures up to 650 $^\circ$ C (S3, mg CO<sub>2</sub> g<sup>-1</sup> rock). Based on these data and corresponding TOC data, the hydrogen index (HI, S2/TOC  $\times$  100), the oxygen index (OI, S3/TOC  $\times$  100) and the production index [PI, S1/(S1 + S2)] were calculated. For P–T samples, the data were already published in Pei (2022).

### Lipid biomarkers

Lipid biomarkers were extracted and analysed at BGR. Only Late Triassic samples are considered in this study, as organic matter in P–T samples from Xiakou has a too high thermal maturity (for more details see *Discussion*) (Pei, 2022).

Details on the extraction, fractionation and subsequent analysis with gas chromatography (GC) – FID or GC-mass spectrometry (MS) can be found in Blumenberg *et al.* (2019). Briefly, organic compounds were extracted with dichloromethane (DCM) using an accelerated solvent extraction device (Dionex ASE-350, Thermo Fisher Scientific, Waltham, MA, USA). About 10 g of each sample was diluted with 22 g sea

sand (Carl Roth GmbH + Co. KG, Karlsruhe, Germany) and extracted and annealed, 4 h at 400°C within an extraction cell. Organic extracts were collected automatically, and elemental sulphur was subsequently removed by granulated, activated copper (10% HCl at 60°C for approximately 1 h). The extracts were fractionated by mid-pressure liquid chromatography into an aliphatic, an aromatic and a polar fraction using isohexane, isohexane/dichloromethane (2/1; v/v) and dichloromethane/methanol (1/1; v/v), respectively. Only the aliphatic fraction was analysed for this study.

The molecular inventory of the aliphatic fractions was analysed with an Agilent 7890 GC (Agilent, Santa Clara, CA, USA) equipped with two 50 m Ultra 1 columns (Agilent; 0.2 mm inner diameter; 0.11 µm film thickness) coupled to either a FID or a triple-quadrupole MS (Agilent 7000). Measurements were carried out as multiple-reaction monitoring (MRM) using parent–daughter scans and in full scan mode (from 50 to 700 amu). The Carbon Preference Index  $CPI = 0.5 \times [(n-C_{25} + n-C_{27} + n-C_{29} + n-C_{31}) / (n-C_{26} + n-C_{28} + n-C_{30} + n-C_{32}) + (n-C_{25} + n-C_{27} + n-C_{29} + n-C_{31}) / (n-C_{24} + n-C_{26} + n-C_{28} + n-C_{30})]$  was calculated based on the obtained data.

### Stable carbon isotope analyses ( $\delta^{13}C_{carb}$ and $\delta^{13}C_{org}$ )

The stable carbon isotopic composition of carbonates was analysed in the Isotope Geology Department at the Geoscience Center at the Georg-August-Universität Göttingen (Germany). Briefly, ca 100 to 600 µg sample material was obtained with a high-precision drill to ensure sampling of individual carbonate microfacies and then measured with a Thermo Scientific Kiel IV carbonate device coupled to a Finnigan DeltaPlus gas isotope mass spectrometer (Thermo Fisher Scientific). Results are reported as delta values relative to Vienna Pee Dee Belemnite (VPDB) reference standard ( $\delta^{13}C_{carb}$ ). Reproducibility was repeatedly tested and generally better than 0.1‰. Please note that  $\delta^{13}C_{carb}$  values of P–T samples were in part already published in Pei *et al.* (2021).

The stable carbon isotopic composition of organic matter was analysed in the Center for Stable Isotope Research and Analysis (KOSI) at the Georg-August-Universität Göttingen (Germany). Briefly, ca 0.5 to 25 mg of decalcified sample material was measured with an Euro EA 3000 elemental analyser (HEKAtech GmbH, Wegberg, Germany) coupled to a Finnigan Delta V

Advantage isotope mass spectrometer (Thermo Fisher Scientific). Results are reported as delta values relative to Vienna Pee Dee Belemnite (VPDB) reference standard ( $\delta^{13}C_{org}$ ). Acetanilide ( $\delta^{13}C = -29.6$ ‰; SD = 0.1) was used for internal calibration. Average standard deviation of  $\delta^{13}C_{org}$  values was 0.3‰. More information on the protocol is provided in Werner *et al.* (1999), and Langel & Dyckmans (2014, 2017). It is important to note that  $\delta^{13}C_{org}$  values of P–T samples reported in this study are not identical to those reported in Pei *et al.* (2021) because they were re-measured for this study.

## RESULTS

### Sedimentological and geochemical characteristics of the Xiakou section, South China

#### *Field observations and microfacies analyses*

The studied interval of the Xiakou section is about 9 m thick, and includes the Changxing, Dalong and Daye formations (Fig. 2). As detailed below, the section mainly comprises grey to black limestones, intercalated with black mudstones (Pei *et al.*, 2021). Several volcanic ash beds/layers occur throughout the section (for example, beds/layers P<sub>15-1</sub>, P<sub>15-3</sub>, T<sub>2</sub>, T<sub>4</sub>, T<sub>13</sub> and T<sub>15</sub>) (Fig. 2). As indicated by XRD analyses, the ash mainly consists of quartz and illite–smectite, agreeing with findings of previous studies (Table S1; Hong *et al.*, 2011; Gao *et al.*, 2013). Notably, some of the ash layers occur at the top of the Dalong Formation, close to the P–T boundary (layers P<sub>15-1</sub> and P<sub>15-3</sub>). These greenish-yellowish layers are 11 cm and 13 cm thick, respectively. Between them, a 14 cm thick, black medium-bedded limestone (layer P<sub>15-2</sub>) containing abundant calcispheres (Fig. 2) was intercalated.

In a previous study, microfacies types (MF) were defined for the relevant part of the Xiakou section (Pei *et al.*, 2021). Briefly summarizing, the uppermost part of the Changxing Formation consists of grey grainstones containing dasyclad green algae and fusulinid foraminifera (MF-1). The Dalong Formation mainly comprises black, laminated micrites with either dolomite rhombs (MF-2) or calcite pseudomorphs after gypsum and *Rectocornuspira* foraminifera (MF-3) (Fig. 5A to C). In addition, the Dalong Formation exhibits interlayers of black, laminated marls with abundant fossil debris (MF-4a) and black, non-laminated marls with calcite and pyrite concretions (MF-4b) (Figs 5D and 6E), as



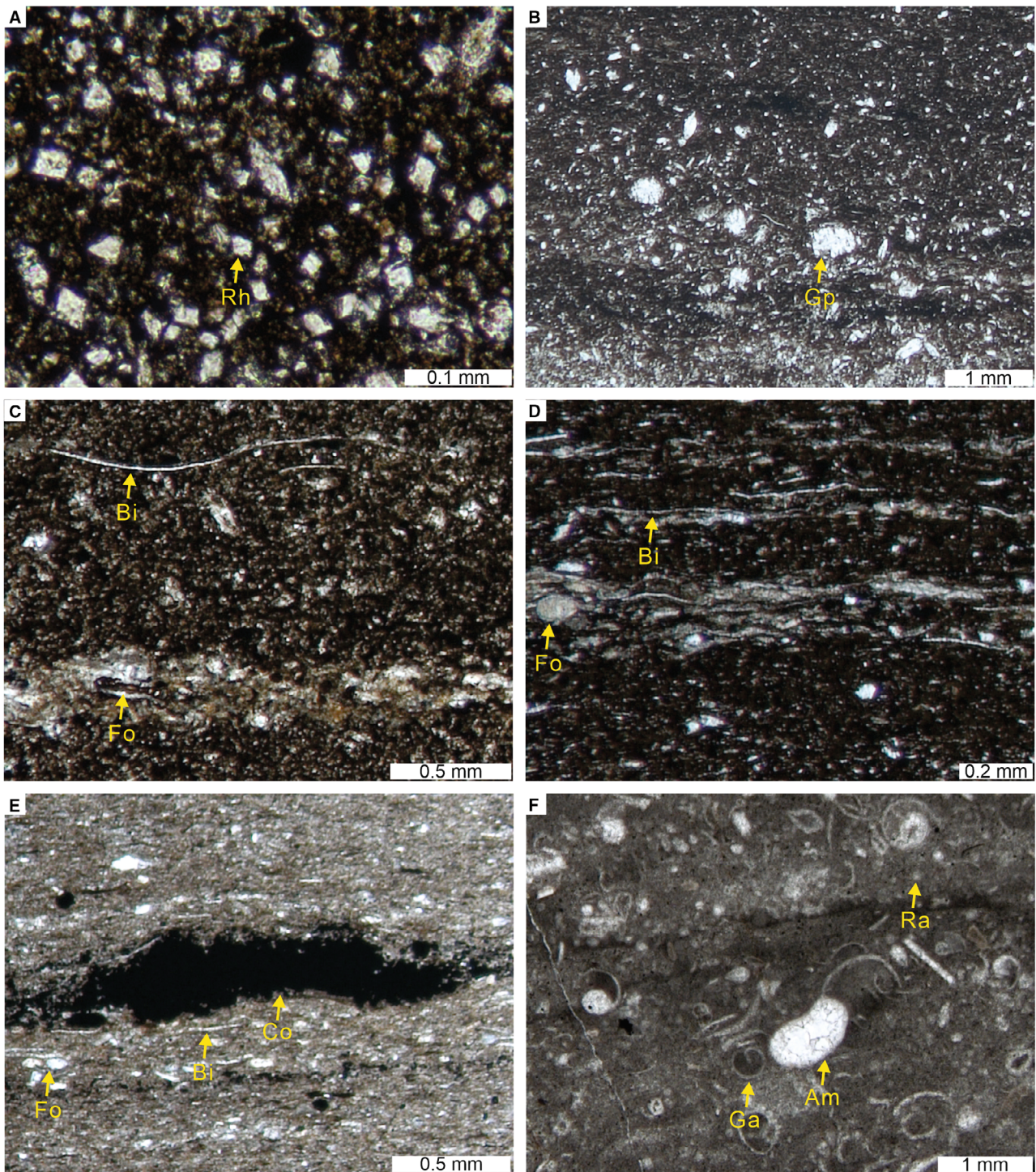


**Fig. 5.** Thin section photomicrographs (plane polarized light) of microfacies (MF) at Xiakou. (A) MF-2, black, laminated micrites with dolomite rhombs (Rh). (B) and (C) MF-3, black, laminated micrites with calcite pseudomorphs after gypsum (Gp) and *Rectocornuspira* foraminifera (Fo). Thin-shelled bivalves (Bi) were observed. (D) MF-4a, black, laminated marls with abundant fossil debris, for example, thin-shelled bivalves (Bi) and small benthic foraminifera (Fo). (E) MF-4b, black, non-laminated marls with calcite and pyrite concretions (Co). Fragmented thin-shelled bivalves (Bi) and small benthic foraminifera (Fo) were noticed. (F) MF-7, grey floatstone to wackestone containing ammonoids (Am). Gastropods (Ga) and radiolarians (Ra) were displayed.

well as black, non-laminated micrites with abundant calcispheres at the top (MF-5) (Fig. 6A and B). The overlying Daye Formation consists of grey,

non-laminated micrite with dolomite rhombs (MF-6) and grey, floatstones to wackestones containing ammonoids (MF-7) (Fig. 5F).

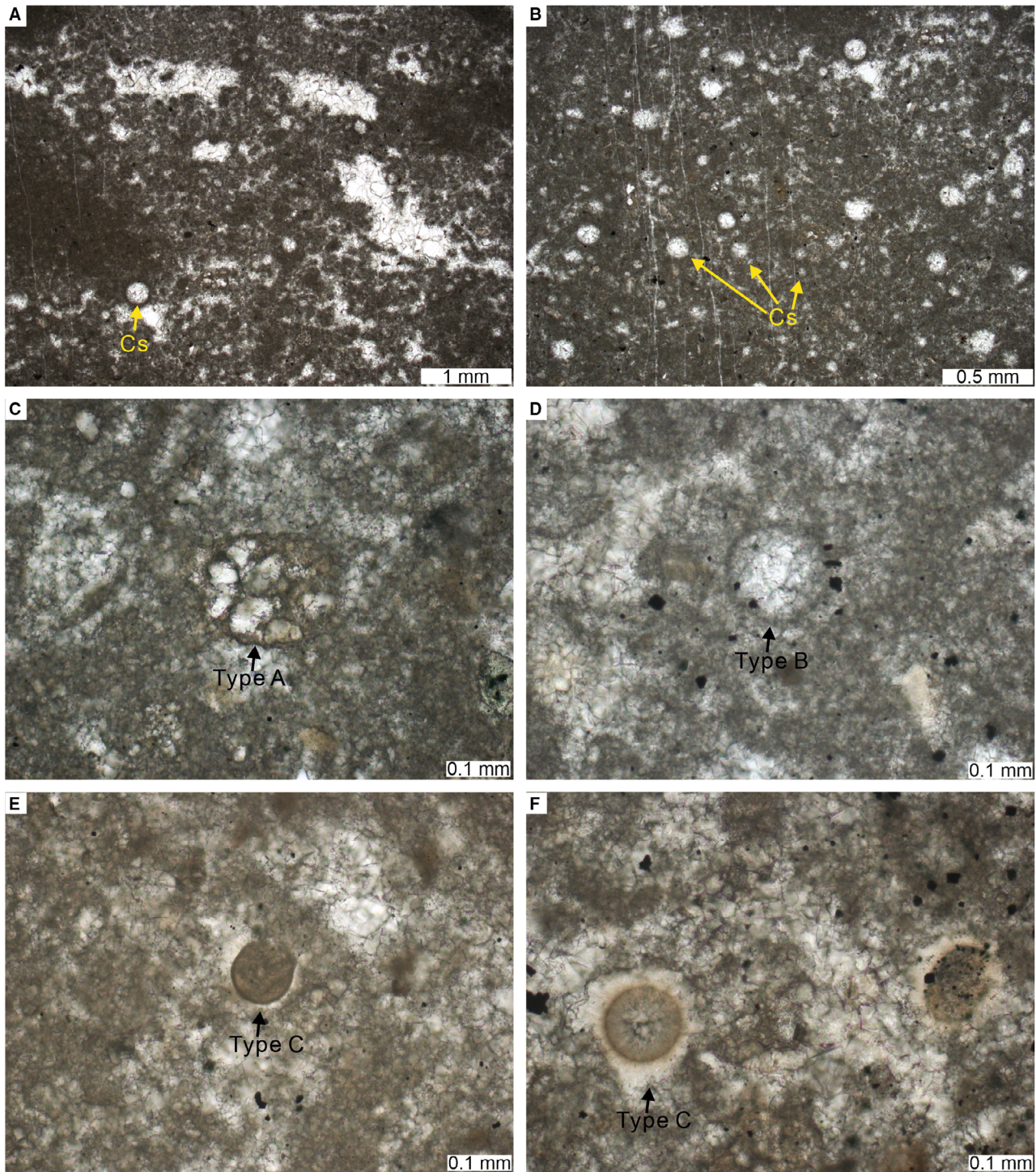


**Fig. 6.** Thin section photomicrographs (plane polarized light) of MF-5 (black, non-laminated micrites with abundant calcispheres: layer P<sub>15-2</sub>) at Xiakou. (A) and (B) This facies is characterized by copious peloidal textures with abundant calcispheres (Cs). Three types of calcispheres were observed. Each type exhibits thin micritic walls. (C) Type A encloses sparite with clear grain boundaries. (D) Type B encloses sparite with indistinct grain boundaries. (E) and (F) Calcispheres of type C are filled with micrite and their walls are encrusted by blocky calcite.

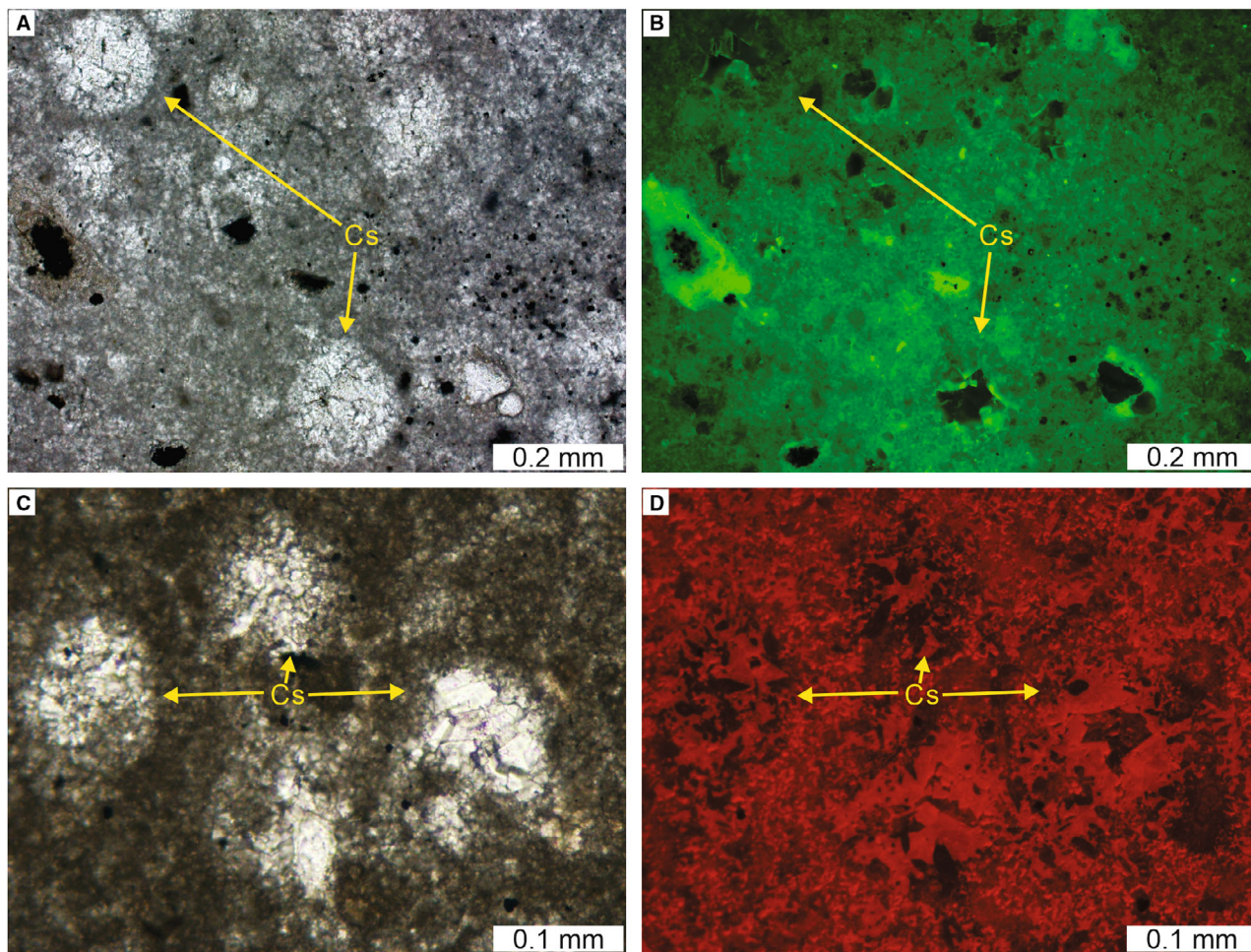


**Fig. 7.** (A) Thin section photomicrograph (plane polarized light) and (B) corresponding epifluorescence microscopy image of MF-5 (layer P<sub>15-2</sub>) at Xiakou. The matrix exhibits a relatively strong green fluorescence. In contrast, the sparite within calcispheres (Cs) of type B shows a relatively dull green fluorescence. (C) Thin section photomicrograph (plane polarized light) and (D) corresponding cathodoluminescence microscopy image of MF-5 (layer P<sub>15-2</sub>). A patchy cathodoluminescence was observed.

The calcisphere-rich MF-5 is restricted to layer P<sub>15-2</sub> of the Dalong Formation and appears to be particularly interesting for several reasons. First, the matrix of MF-5 is characterized by copious peloidal textures (Fig. 6A and B), which exhibits a relatively strong green fluorescence (Fig. 7A and B) and a patchy cathodoluminescence (Fig. 7C and D). Raman spectroscopy reveals that the matrix not only consists of calcite, but also comprises organic matter (Fig. 8A and B). Second, it contains abundant calcispheres, which range from *ca* 50  $\mu\text{m}$  to 300  $\mu\text{m}$  in diameter and exhibit thin micritic walls. Three calcisphere types (types A to C) can be distinguished (Fig. 6C to F). Calcispheres of type A and B enclose sparite with clear and indistinct grain boundaries, respectively (Fig. 6C and

D). The sparite within calcispheres of type B shows a relatively dull green fluorescence (Fig. 7A and B) and a patchy cathodoluminescence (Fig. 7C and D). Calcispheres of type C, in contrast, are filled with micrite and their walls are encrusted by blocky calcite (Fig. 6E and F). Raman spectroscopy revealed that the internal fillings of all calcisphere types consist of calcite, while their micritic walls additionally contain organic matter (Fig. 8C and F).

#### *Bulk geochemical characterization*

The TIC and TOC contents are highly variable (Table 1; Fig. 9; Pei *et al.*, 2021, table 1, fig. 2). Carbonate contents vary between *ca* 11.3 wt.% and 91.9 wt.% (beds P<sub>14</sub> and P<sub>1</sub>, respectively), with an average value of 65.5 wt.%. TOC contents range

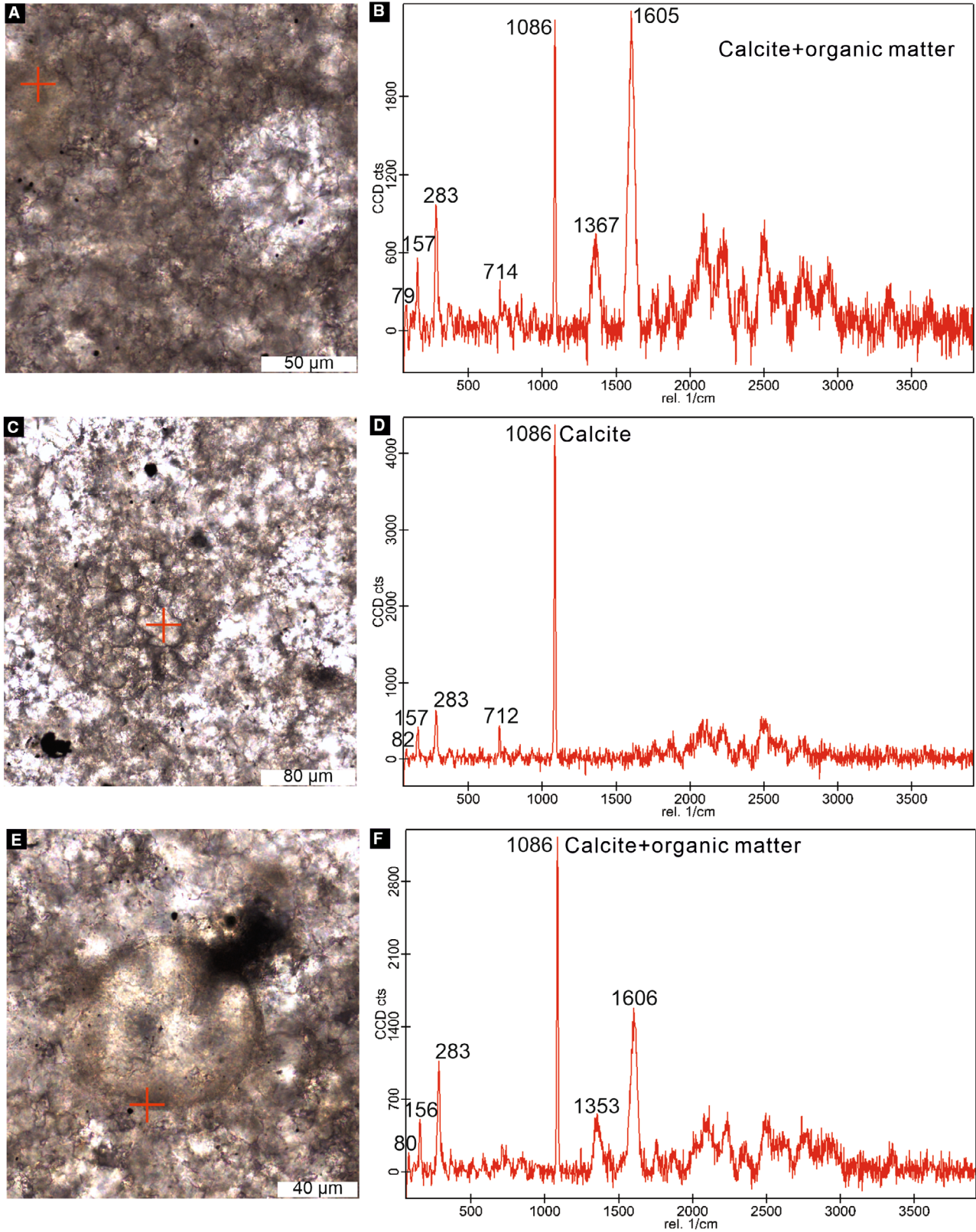


**Fig. 8.** Thin section photomicrographs (plane polarized light) (A), (C) and (E) and Raman spectroscopy data (single spectra) (B), (D) and (F) of MF-5 (layer P<sub>15-2</sub>) at Xiakou. (A) and (B) The matrix mainly consists of calcite with organic matter. (C) to (F) The internal fillings of all calcisphere types consist of calcite, while their micritic walls additionally contain organic matter. The unmarked peaks in (B), (D) and (F) are attributed to fluorescence interference.

**Table 1.** Bulk geochemical data, including carbonate (wt.%), total organic carbon (TOC, wt.%), temperature at maximum yields of S2 hydrocarbons ( $T_{\max}$ , °C), quantities of free hydrocarbons (S1, mg HC g<sup>-1</sup> rock), hydrocarbons yielded from labile kerogen (S2, mg HC g<sup>-1</sup> rock), the CO<sub>2</sub> generated from organic carbon at higher temperatures up to 650°C (S3, mg CO<sub>2</sub> g<sup>-1</sup> rock), the hydrogen index (HI; S2/TOC × 100), the oxygen index (OI; S3/TOC × 100) and the production index (PI; S1/(S1 + S2)) (partially modified from Pei *et al.*, 2021; Pei, 2022). Stable isotopic data, including carbonate carbon stable isotopic compositions ( $\delta^{13}C_{\text{carb}}$ , ‰) and organic carbon stable isotopic compositions ( $\delta^{13}C_{\text{org}}$ , ‰) (partially modified from Pei *et al.*, 2021). P, Permian; T, Triassic; R, Rhaetian; S, Sinemurian.

Section	Sample	Carbonate	TOC	$T_{\max}$	S1	S2	S3	HI	OI	PI	$\delta^{13}C_{\text{carb}}$	$\delta^{13}C_{\text{org}}$
Xiakou	P <sub>1</sub>	91.9	0.30	–	–	–	–	–	–	–	4.2	–26.5
	P <sub>2</sub>	57.4	2.91	444	0.79	4.02	0.15	138	5	0.16	1.4	–26.5
	P <sub>3</sub>	89.3	0.62	–	–	–	–	–	–	–	1.0	–26.4
	P <sub>4</sub>	67.8	1.85	–	–	–	–	–	–	–	–	–26.5
	P <sub>5</sub>	80.1	0.74	447	0.25	0.76	0.20	103	27	0.25	2.4	–25.7
	P <sub>7</sub>	83.5	0.82	–	–	–	–	–	–	–	2.0	–26.1
	P <sub>8</sub>	20.5	4.18	–	–	–	–	–	–	–	2.0	–26.1
	P <sub>9</sub>	80.8	0.92	–	–	–	–	–	–	–	–	–26.1
	P <sub>10</sub>	20.3	3.59	–	–	–	–	–	–	–	1.8	–26.0
	P <sub>11</sub>	81.2	0.81	–	–	–	–	–	–	–	1.5	–26.1
	P <sub>12</sub>	17.6	3.76	449	2.08	5.79	0.10	154	3	0.26	1.5	–26.7
	P <sub>14</sub>	11.3	1.08	440	0.39	0.94	0.13	87	12	0.29	1.7	–25.8
	P <sub>15-2</sub>	87.1	0.11	–	–	–	–	–	–	–	1.6	–26.0
	P <sub>16</sub>	69.9	0.32	–	–	–	–	–	–	–	1.1	–25.1
	T <sub>1</sub>	67.1	0.21	–	–	–	–	–	–	–	0.9	–26.5
	T <sub>3</sub>	71.0	0.44	–	–	–	–	–	–	–	–	–27.0
	T <sub>5</sub>	67.6	0.25	–	–	–	–	–	–	–	–	–27.4
	T <sub>6</sub>	69.9	0.23	–	–	–	–	–	–	–	0.8	–26.0
T <sub>8</sub>	53.9	0.17	–	–	–	–	–	–	–	–	–23.9	
T <sub>11</sub>	74.6	0.16	–	–	–	–	–	–	–	–	–25.7	
T <sub>12</sub>	75.5	0.25	–	–	–	–	–	–	–	0.7	–25.4	
T <sub>14</sub>	83.0	0.10	–	–	–	–	–	–	–	–	–26.3	
T <sub>16</sub>	68.8	0.30	–	–	–	–	–	–	–	–	–27.6	
T <sub>17</sub>	65.3	0.18	–	–	–	–	–	–	–	1.0	–25.9	
T <sub>18</sub>	82.0	0.19	–	–	–	–	–	–	–	1.1	–27.4	
Lahnwies-Syncline	R <sub>1</sub>	69.9	1.24	–	–	–	–	–	–	–	0.9	–27.8
	R <sub>2</sub>	71.2	1.52	427	0.05	6.06	0.47	439	34	0.01	–	–29.6
	R <sub>3</sub>	58.7	6.18	427	0.52	40.06	1.03	647	17	0.01	1.8	–30.1
	R <sub>4</sub>	79.7	0.69	–	–	–	–	–	–	–	0.9	–28.0
	R <sub>5</sub>	70.2	4.73	426	0.35	31.87	1.12	590	21	0.01	0.6	–30.0
	R <sub>6</sub>	78.9	3.33	425	0.11	17.16	0.93	515	28	0.01	–	–
	R <sub>7</sub>	75.3	5.66	426	0.26	33.44	1.39	591	25	0.01	–	–
	R <sub>8</sub>	88.2	0.21	–	–	–	–	–	–	–	–4.6	–26.5
	S <sub>1</sub>	90.0	–	–	–	–	–	–	–	–	0.6	–

between 0.10 wt.% and 4.18 wt.% (beds T<sub>14</sub> and P<sub>8</sub>, respectively), with an average value of 0.98 wt.%.

Programmed pyrolysis ('Rock-Eval') derived  $T_{\max}$  values vary between 440°C and 449°C (Table 1). HI and OI values range from 87 to 154 mg HC g<sup>-1</sup> TOC and from 3 to 27 mg CO<sub>2</sub> g<sup>-1</sup> TOC, respectively. The production index (PI) values range between 0.16 and 0.29 (Table 1; Pei, 2022).

**Stable carbon isotopes ( $\delta^{13}C_{\text{carb}}$  and  $\delta^{13}C_{\text{org}}$ )**  
 $\delta^{13}C_{\text{carb}}$  values range between 0.7‰ and 4.2‰ (beds T<sub>12</sub> and P<sub>1</sub>, respectively), with an average

value of 1.6‰.  $\delta^{13}C_{\text{carb}}$  value is highest at the base of the section (4.2‰ in bed P<sub>1</sub>) and then decreases significantly towards the top (1.1‰ in bed T<sub>18</sub>). This trend is only interrupted by bed P<sub>5</sub>, which shows a higher  $\delta^{13}C_{\text{carb}}$  value of 2.4‰ (Table 1; Fig. 9; Pei *et al.*, 2021, table 2, fig. 10).

$\delta^{13}C_{\text{org}}$  values range between –27.6‰ and –23.9‰ (beds T<sub>16</sub> and T<sub>8</sub>, respectively), with an average value of –26.2‰. Section upwards,  $\delta^{13}C_{\text{org}}$  generally shows a slightly increasing trend (Table 1; Fig. 9; Pei *et al.*, 2021, table 1, fig. 2).

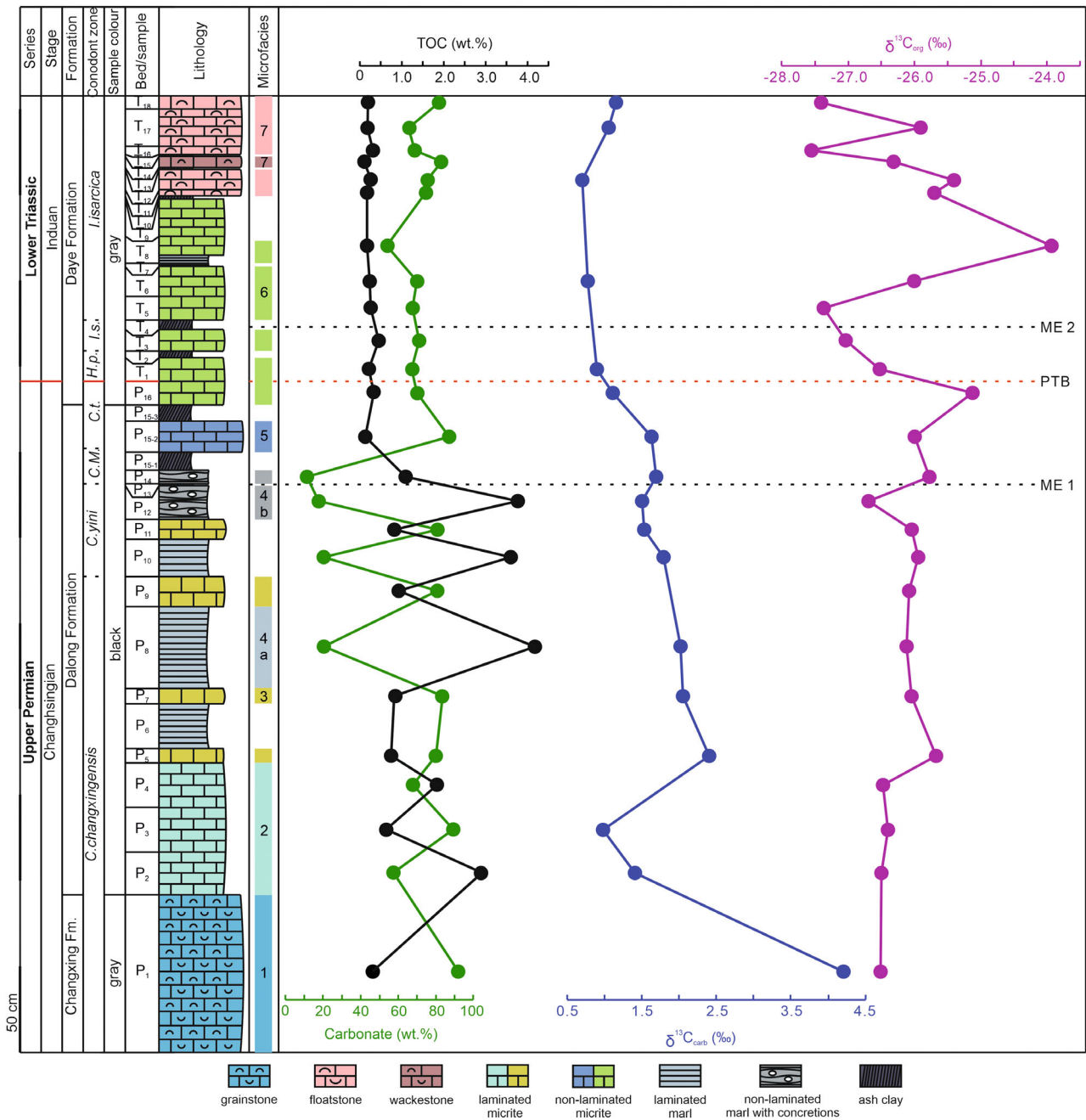


**Fig. 9.** Profiles of bulk geochemical and stable isotopic data at Xiakou (modified from Pei *et al.*, 2021), including Carbonate (wt.%), TOC (wt.%),  $\delta^{13}C_{carb}$  (‰) and  $\delta^{13}C_{org}$  (‰). ME 1, Mass extinction 1 (after Song *et al.*, 2013); PTB, Permian–Triassic boundary (after Zhao *et al.*, 2013); ME 2, Mass extinction 2 (after Song *et al.*, 2013); C.m., *Clarkina meishanensis*; C.t., *Clarkina taylorae*; H.p., *Hindeodus parvus*; L.s., *Isarcicella staeschei*.

**Sedimentological and geochemical characteristics of the Lahnewies Syncline Section, Northern Calcareous Alps**

*Field observations and microfacies analyses*  
 The combined Lahnewies Syncline section is about 60 m thick. No volcanic ash beds/layers

were recorded, consistent with XRD data analyses (Table S1; Fig. 4). The section begins with the Hochalm Member, consisting of framestones characterized by corals and coralline sponges that are associated with green algae (*Dasycladaceae*) and large molluscs (*Neomegalodon*)

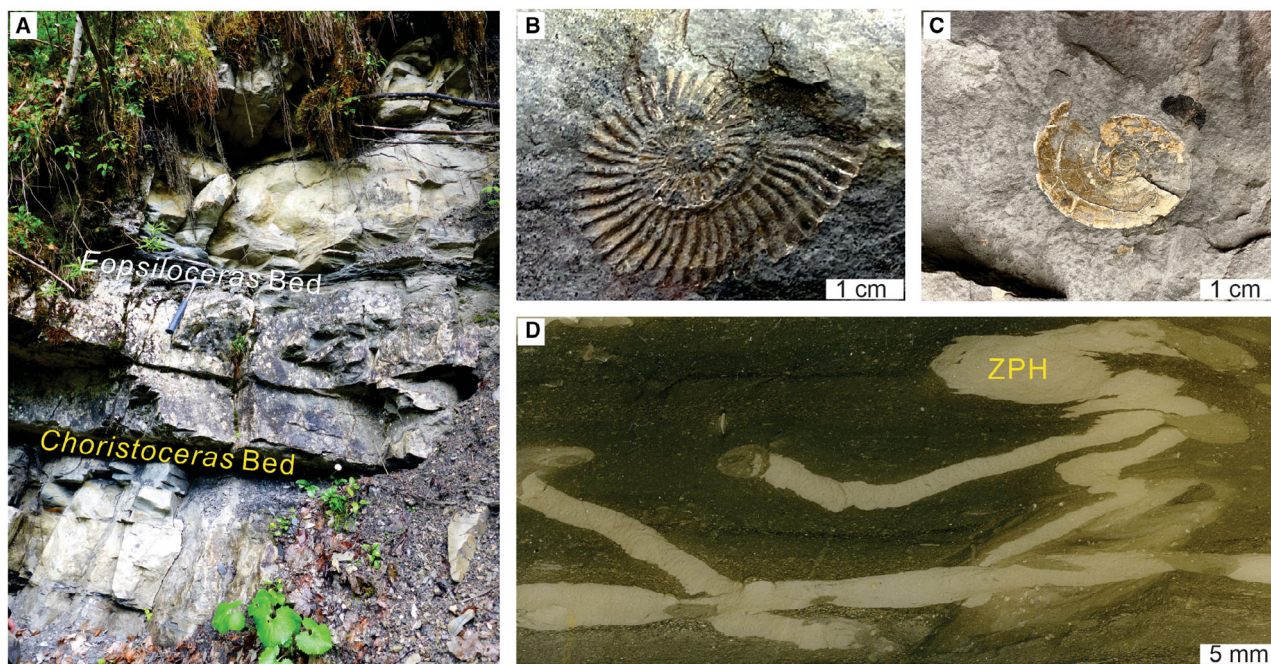


**Fig. 10.** (A) *Choristoceras* Bed and *Epsilonoceras* Bed in the upper part of the Eiberg Member, the Lahnewies Syncline section (Lahnewies Creek part). Hammer for scale is ca 30 cm long. (B) The *Choristoceras* Bed is enriched in juvenile individuals of the ammonoid *Choristoceras* (Gümbel, 1861; Reitner, 1978). (C) The *Epsilonoceras* Bed is abundant in *Epsilonoceras planorboides* (Gümbel, 1861), unique for the section. (D) Enriched *Zoophycos* (ZPH) burrowing traces are exhibited in the upper part of the *Epsilonoceras* Bed.

(Schäfer, 1979; Bernecker *et al.*, 1999). The above Eiberg Member is marked by two distinct beds rich in organic matter (*Choristoceras* Bed and *Epsilonoceras* Bed) (Figs 4 and 10A). The lower bed is characterized by a mass occurrence of juvenile individuals of the ammonoid *Choristoceras* (Fig. 10B; Gümbel, 1861; Reitner, 1978). The upper bed contains the ammonoids *Epsilonoceras planorboides* and *Choristoceras ammonitiforme* (Fig. 10C; Gümbel, 1861). Furthermore, this bed also preserves a diverse bivalve community, dominated by the thin-shelled pectinid *Agerchlamys*. The ammonoid *C. ammonitiforme* indicates a stratigraphic position below the *C. marshi* zone (Wiedmann *et al.*, 1979; Krysytyn, 1987; Karl *et al.*, 2014; Galbrun *et al.*, 2020). The mass occurrence of relatively well-preserved *E. planorboides* specimens in the upper bed is also notable because this phylloceratid ammonite is generally rare and restricted to the Lahnewies Syncline. The originally aragonitic shells of *E. planorboides* individuals are diagenetically dissolved and have not been replaced, whereas the periostracum is mostly preserved in its original form. If freshly exposed, *E. planorboides* typically exhibits a golden

colour, while it appears white in specimens that are exposed to air.

The *Epsilonoceras* Bed consists of mudstones to wackestones. In the upper part, the bed locally contains abundant framboidal pyrite and shows evidence for significant bioturbation by *Zoophycos* (Fig. 10D). The micrite mainly contains globular nanofossils such as *Prinsiosphaera triassica* (abundant) (Figs 11A, 11B and 12A to C) and *Orthopithonella* (subordinate), both of which were interpreted as dinoflagellate cysts (Jafar, 1983; Janofske, 1987, 1992; Demangel *et al.*, 2020). Coccolith remains are also abundant but poorly preserved due to diagenesis (Fig. 11A and B). However, most coccoliths could be assigned to *Archaeozygodiscus*, *Crucirhabdus* and *Cleosphaera* (Janofske, 1987; Bown, 1987a,b; Bown *et al.*, 2004). Occasionally, other nannoliths such as *Conusphaera* (Jafar, 1983; Janofske, 1987, 1992) as well as spherical aggregates of calcite crystal plates occurred, which probably also represented mineralized haptophytes. Taken together, calcified planktonic algae are the major constituent of the carbonate sediment.

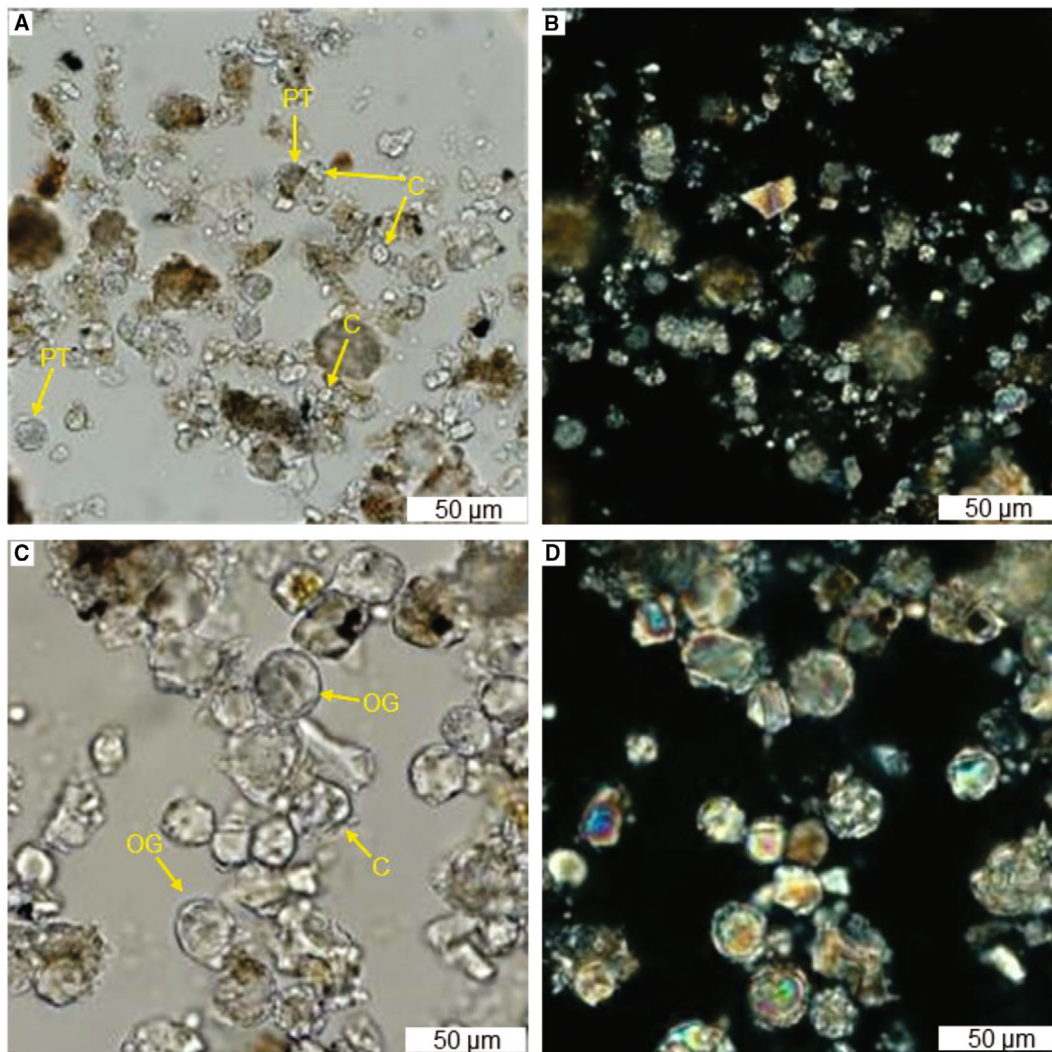


**Fig. 11.** Thin section photomicrographs (smear slides) of nannoplankton fossils, the Lahnewies Syncline section (Lahnewies Creek part). (A) Various nannoplankton fossils in the *Epsilonoceras* Bed (samples R<sub>2</sub>, R<sub>3</sub>). The bed contains abundant *Prinsiosphaera triassica* (PT), interpreted as dinoflagellate cysts (Jafar, 1983; Janofske, 1987, 1992; Demangel et al., 2020) and diagenetically altered coccolith remains (C), assigned to *Archaeozygodiscus*, *Crucirhabdus*, and *Cleosphaera* (Janofske, 1987; Bown, 1987a,b; Bown et al., 2004). (B) Same photograph as (A) under crossed nicols. (C) Various nannoplankton fossils in the top layer of the T-Bed (sample R<sub>6</sub>). The T-Bed contains abundant *Orthopithonella geometrica* (OG), and diagenetically altered coccolith remains (C). (D) Same photograph as (C) under crossed nicols.

A few metres above the *Epsilonoceras* Bed, the ca 50 to 100 cm thick T-Bed follows, which marks the top of the Eiberg Member (Figs 4 and 13) and consists of mudstones to wackestones (Fig. 14A and B). Similar to the *Epsilonoceras* Bed, the T-Bed contains *Zoophycos* burrows, but these traces successively disappear towards the top part (Fig. 13E). The T-Bed also contains the ammonoid *C. marshi* in the top layer (Fig. 14C), which confirms a late Rhaetian age.

Furthermore, the T-Bed preserves diverse assemblages of epibyssate pectinid bivalves (*Agerchlamys* sp., *Pseudolima* sp.) (Fig. 14D and E), similar to other locations in the Northern Calcareous Alps (McRoberts et al., 2008, 2012). Notably, the thin shells of the bivalves are commonly intact and articulated, and often consist of primary aragonite (Fig. 14A). The only abundant infaunal organisms are undescribed linguroid brachiopods (*Lingularia*?) (Fig. 14F; Sýkora



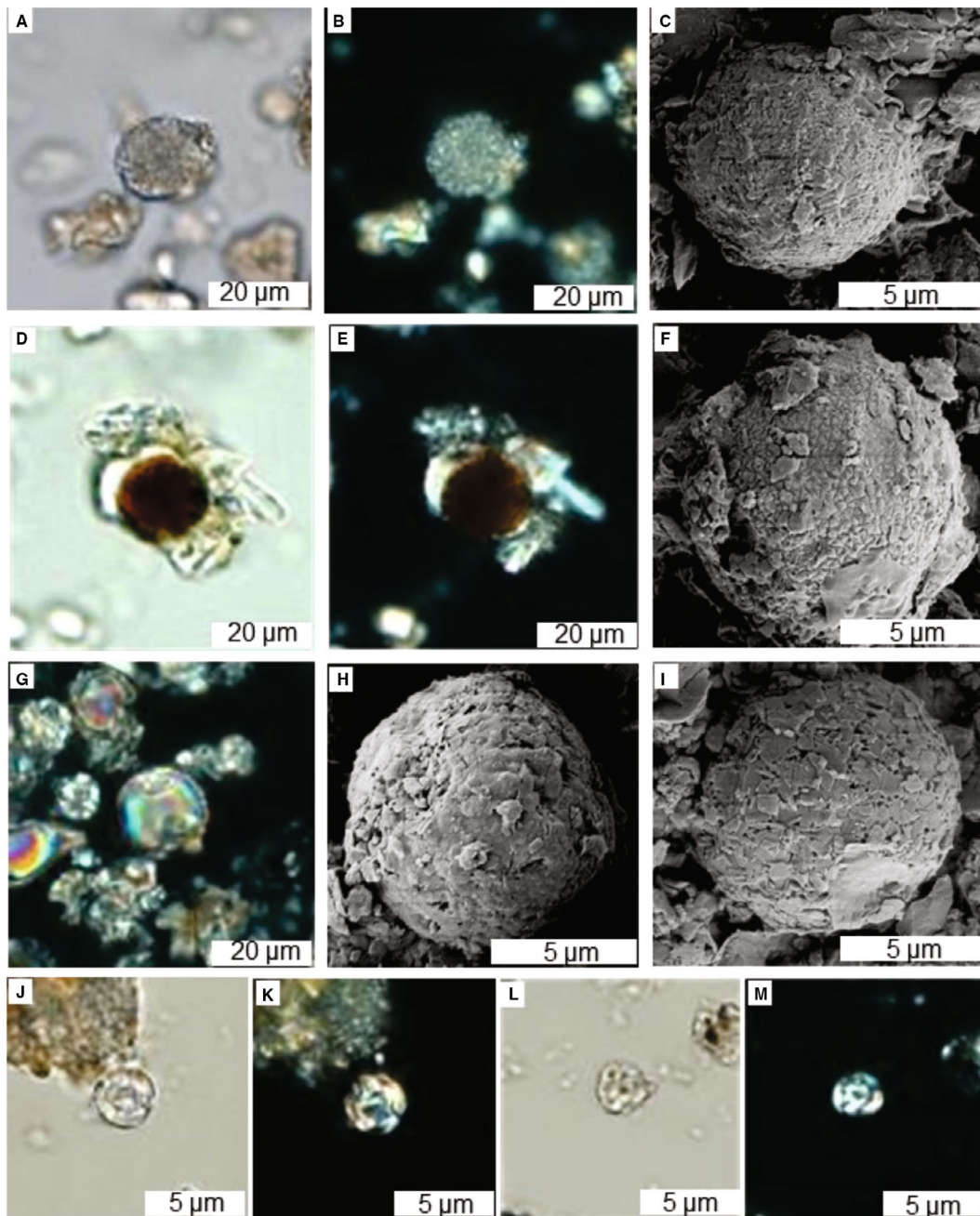


**Fig. 12.** Thin section photomicrographs (smear slides) (A, B, D, E, G, J and M) and (C, F, H and I) field emission scanning electron microscopy (FE-SEM) images of nannoplankton fossils, the Lahnewies Syncline section (Lahnewies Creek part). (A) to (C) *Prinsiosphaera triassica* in the *Epsilonoceras* Bed (samples R<sub>2</sub>, R<sub>3</sub>). (A) Transmitted light. (B) Crossed nicols. (C) FE-SEM. Filled spheres were composed of clusters of calcite plates arranged in a cross lamellae structure. (D) to (F) *Orthopithonella geometrica* in the top layer of the T-Bed (sample R<sub>6</sub>). (D) Transmitted light, the inner part of the hollow sphere is an organic cyst. (E) Crossed nicols. (F) FE-SEM, the prismatic calcite rhombohedrons are shown. (G) to (I) *Obliquipithonella rhombica* in the top layer of the T-Bed (sample R<sub>6</sub>). (G) Crossed nicols, a clear apophyle is exhibited. (H) FE-SEM, a clear apophyle is also exhibited. (I) FE-SEM, parallel, tangentially orientated calcite crystals are exhibited. (J) to (M) Coccoliths in the top layer of the T-Bed (sample R<sub>6</sub>). (J) and (K) Circular heterococcolith, attributed to *Cleosphaera tripartita*. (J) Transmitted light. (K) Crossed nicols. (L) and (M) *Archaeozygodiscus* sp. (L) Transmitted light. (M) Crossed nicols.



**Fig. 13.** (A) and (B) T-Bed marks the top of the Eiberg Member, the Lahnewies Syncline section (Lahnewies Creek part). It is followed by the Tiefengraben Member (TG-M). Pink coloured Schattwald Bed, belonging to the TG-M, is exhibited. (C) and (D) Core of the top of T-Bed. (E) The T-Bed exhibits *Zoophycos* burrows (ZPH; sample R<sub>4</sub>), but these traces successively disappear towards the top part. The upper part exhibits an enrichment of organic matter and a decrease of *Zoophycos* (sample R<sub>5</sub>). The top layer (sample R<sub>6</sub>) contains abundant organic matter. Hammer = 40 cm; people are ca 1.8 m tall.

et al., 2011). In the top layer of the T-Bed, fish remains are preserved (Fig. 14G).

The top layer of the T-Bed contains abundant nannofossils, particularly *Orthopithonella geometrica* (dominant) (Figs 11C, 11D and 12D to F) and *Obliquipithonella rhombica* (less abundant) (Fig. 12G to I). Moreover, the micrites mainly consist of diagenetically altered remains of calcified planktonic algae such as calcispheres (for example, *Prinsiophera*, *Orthopithonella*) and coccoliths (for example, *Cleosphaera tripartita*, *Archaeozygodiscus* sp.) (Figs 11C, 11D and 12J to M).

The Tiefengraben Member begins above the T-Bed and consists of black mudstones that contain only few microfossils (for example, the ostracod *Bairdia* sp., and the unusual foraminifer *Praegubkinella* sp.) but no nannofossils. In the lower part, the Tiefengraben Member locally exhibits organic-lean carbonate concretions (Fig. 15A and B). The overlying Schattwald Beds are characterized by pink colour, carbonate-poor mudstones with an absence of fossils (Fig. 15C). The Breitenberg Member atop, in contrast, consists of wackestones and

contains abundant fossils of demosponges, radiolarians and benthic foraminifera (Fig. 15D and E). Particularly noteworthy is the ammonoid *Psiloceras naumanni* (Fig. 15F to H), which is indicative for the *Calliphyllum* zone, and hence a Hettangian age.

The following Scheibelberg Formation comprises grey bedded limestones with chert nodules and contains abundant fossils, including ammonites, radiolarians, foraminifera (for example, *Involutina* sp.), and spicules of siliceous sponges (Fig. 16A to D). The ammonoid *Schlotheimia* sp. (Fig. 16B) indicates a late Hettangian age.

#### Bulk geochemical characterization

Total organic carbon contents of the analysed samples vary between 0.21 wt.% and 6.18 wt.%, while TIC contents range between ca 60 wt.% and 90 wt.% (Table 1; Fig. 4). Programmed pyrolysis yields  $T_{\max}$  values <430°C (Table 1). OI values are relatively low for all samples (<35 mg CO<sub>2</sub> g<sup>-1</sup> TOC), while HI values are mostly rather high (>435 mg HC g<sup>-1</sup> TOC). PI values are around 0.01 (Table 1).

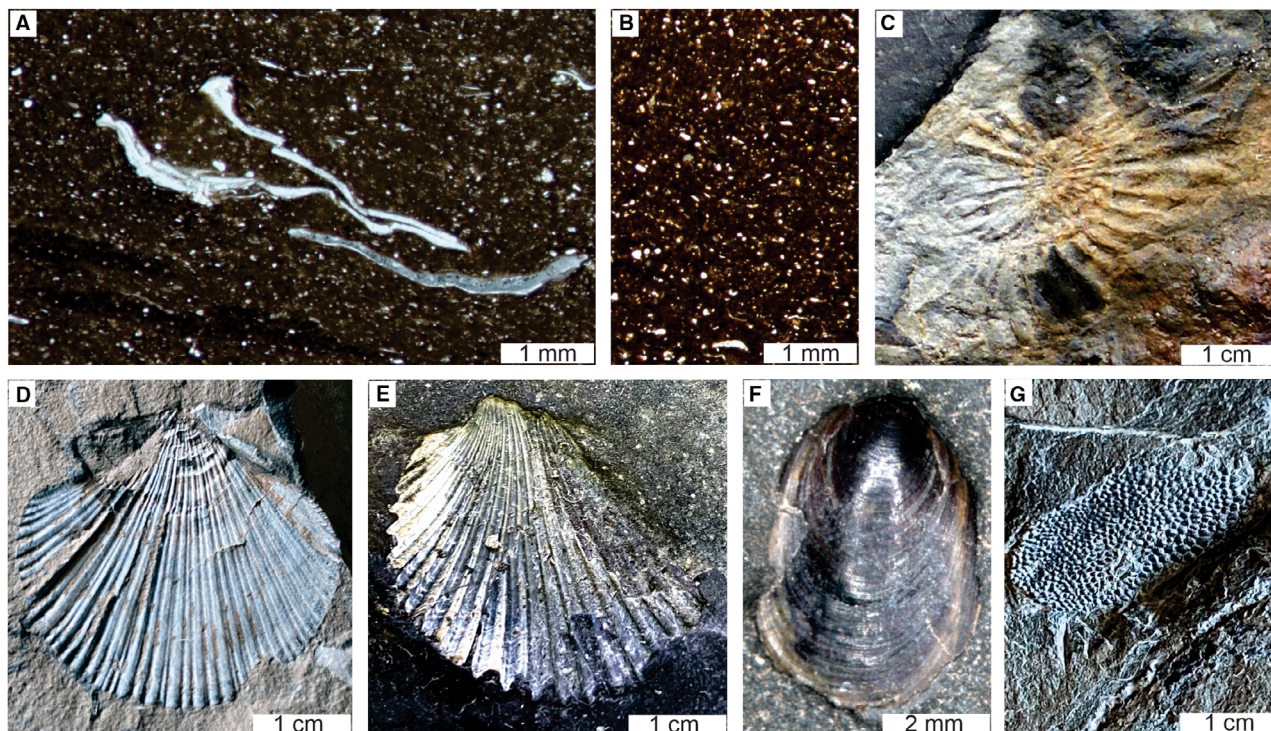


**Fig. 14.** (A) and (B) T-Bed consists of mudstones to wackestone. Notably, the thin shells of the bivalves are commonly intact and articulated, and often consist of primary aragonite. (C) Ammonoid *Choristoceras marshi*, in the top layer of the T-Bed (sample R<sub>6</sub>), the Lahnewies Syncline section (Lahnewies Creek part), confirming a late Rhaetian age. (D) to (E) Epibyssate pectinid bivalves *Agerchlamys* cf. *textoria* and *Pseudolima* cf. *hettangiensis*, in the top layer of the T-Bed. (F) Undescribed linguloid brachiopods (*Lingularia*?) (Sýkora *et al.*, 2011), in the top layer of the T-Bed. (G) Fish remains, in the top layer of the T-Bed.

### Lipid biomarkers

The aliphatic fractions of all studied TOC-rich samples contain abundant *n*-alkanes as well as acyclic head-to-tail linked isoprenoids, such as pristane and phytane (Fig. 17A). Furthermore, a clear odd-over-even predominance is detected between *n*-C<sub>24</sub> and *n*-C<sub>32</sub> (CPI = 1.7–2.7; Table 2). Samples R<sub>5</sub> and R<sub>6</sub> from the T-Bed contain remarkably high abundances of *n*-C<sub>37–39</sub> (Fig. 17B).

The samples preserve abundant hopanes and hopenes, which are dominated by 17β(H), 21β(H), 22*R* isomers. Among steroids, two series of diaster-13(17)-enes and 4-methyldiaster-13(17)-enes (Volkman *et al.*, 2015) are most abundant. The major diasterene was tentatively identified as 4-methyl-24-ethylcholest-13(17)-ene. Because standard compounds were not available, and mass spectra might be similar (Volkman *et al.*, 2015), this compound may also represent a 4,23,24-trimethylated equivalent, which is a dinosterane transformation product. Indeed,

dinosteranes were identified by MRM analyses and relative abundances among regular steranes are highest in samples R<sub>5</sub>–R<sub>7</sub> from the T-Bed (Table 2; Fig. 17A).

### Stable carbon isotopes ( $\delta^{13}C_{carb}$ and $\delta^{13}C_{org}$ )

$\delta^{13}C_{carb}$  values vary from –4.6‰ to 1.8‰ (samples R<sub>8</sub> and R<sub>3</sub>, respectively) (Table 1; Fig. 4). The *Epsilonoceras* Bed and the T-Bed both exhibit  $\delta^{13}C_{carb}$  values of ca 1‰, while the Tiefengraben Member is characterized by a significantly lower  $\delta^{13}C_{carb}$  value of –4.6‰ (sample R<sub>8</sub>).

$\delta^{13}C_{org}$  values range between –30.1‰ and –26.5‰ (samples R<sub>3</sub> and R<sub>8</sub>, respectively) (Table 1; Fig. 4). Both the *Epsilonoceras* Bed and T-Bed exhibit low  $\delta^{13}C_{org}$  values of ca –30‰ (Table 1; Fig. 4), which is in the range of the well-documented negative  $\delta^{13}C_{org}$  excursion at the T–J boundary (Ruhl *et al.*, 2010, 2011; Ruhl & Kürschner, 2011). In the Tiefengraben Member,  $\delta^{13}C_{org}$  value is higher (–26.5‰ in sample R<sub>8</sub>) (Table 1; Fig. 4).

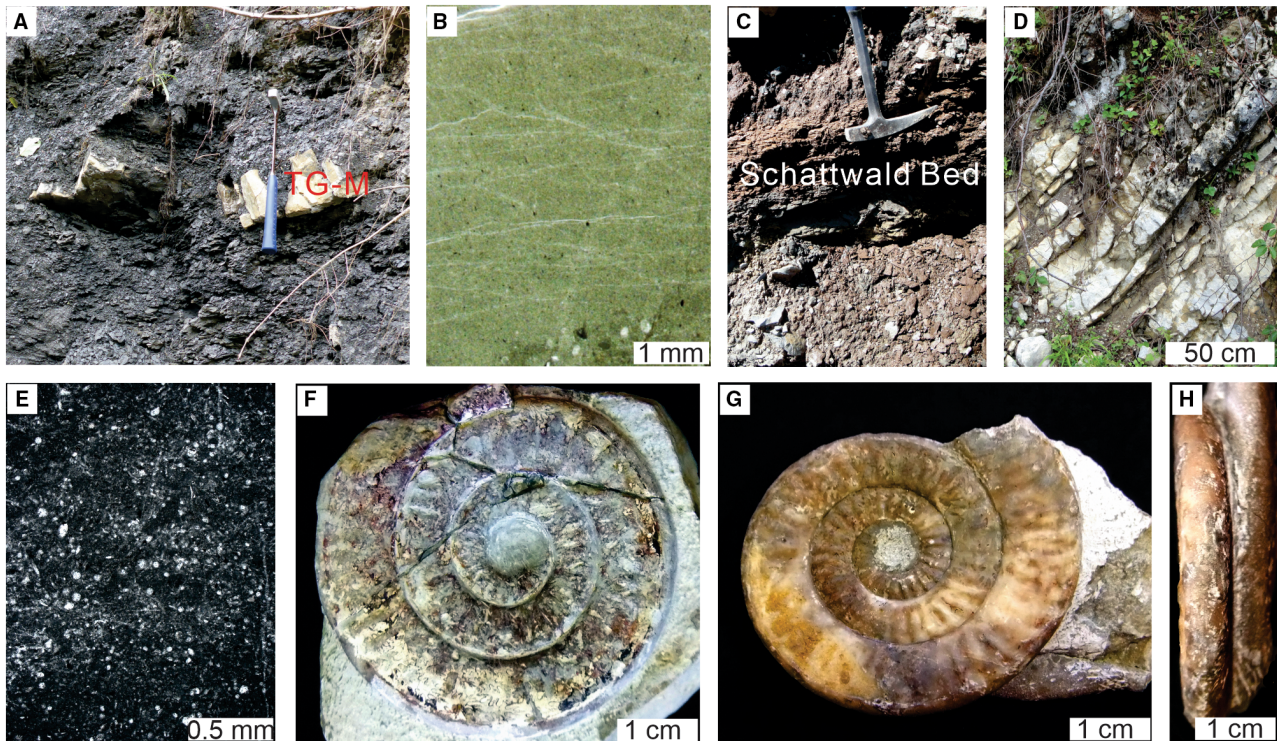


**Fig. 15.** (A) Tiefengraben Member (TG-M) locally exhibits organic-lean carbonate concretions (Sample R<sub>8</sub>), the Lahnnewies Syncline section (Nudelgraben Creek part). (B) The carbonate part (TG-M) (Sample R<sub>8</sub>) is mainly micrite, devoid of fossils. (C) The overlying Schattwald Beds are characterized by pink carbonate-poor mudstones with an absence of fossils, the Lahnnewies Syncline section (Nudelgraben Creek part). (D) Breitenberg Member atop, the Lahnnewies Syncline section (Lahnnewies Creek part). (E) Consists of wackestones and contains abundant fossils of demosponges, radiolarians and benthic foraminifera. (F) to (H) Ammonoid *Psiloceras naumanni*, *Calliophyllum* Zone, Hettangian, in the Breitenberg Member. (H) External view of the same ammonoid as that in (G). Hammer = 40 cm.

## DISCUSSION

### Organic matter preservation

Sedimentary organic records might be compromised by post-depositional processes, particularly through thermal degradation during burial (Peters *et al.*, 2005; Mißbach *et al.*, 2016). Therefore, the thermal maturity of organic matter has to be critically assessed prior to further geobiological interpretations (Love & Zumberge, 2021). Programmed pyrolysis data are powerful means for such assessments, but can only be considered robust if TOC is  $\geq 0.2$  wt.% and S<sub>2</sub> is  $> 0.2$  mg HC g<sup>-1</sup> rock (Peters, 1986; Peters & Cassa, 1994). All samples analysed herein meet these criteria and can be considered reliable (Table 1; Pei, 2022).

At Xiakou,  $T_{\max}$  values (440°C to 449°C, mean 445°C; Table 1) indicate early to peak oil window maturity (Peters, 1986; Peters &

Cassa, 1994). However, HI and OI values (87 to 154 mg HC g<sup>-1</sup> TOC and 3 to 27 mg CO<sub>2</sub> g<sup>-1</sup> TOC, respectively; Table 1) evidence a relatively low hydrocarbon generation potential (Peters, 1986; Peters & Cassa, 1994). Correspondingly, PI ranged from 0.16 to 0.29. In a pseudo-van Krevelen diagram (van Krevelen, 1961), the samples are classified as type IV kerogen (inertinite). Because of the high thermal maturity of organic matter, samples from Xiakou are not suitable for lipid biomarker analysis (Pei, 2022).

In the Lahnnewies Syncline section,  $T_{\max}$  values ( $< 430^\circ\text{C}$ ; Table 1) indicate thermally immature organic matter. HI and OI values ( $> 435$  mg HC g<sup>-1</sup> TOC and  $< 35$  mg CO<sub>2</sub> g<sup>-1</sup> TOC, respectively; Table 1) are indicative for type II kerogens that typically form in marine environments (Peters, 1986; Peters & Cassa, 1994). The low thermal maturity of organic matter is in good accordance with PI  $< 0.1$  and CPIs  $> 1$  (Tables 1 and 2). Because of the low thermal maturity of

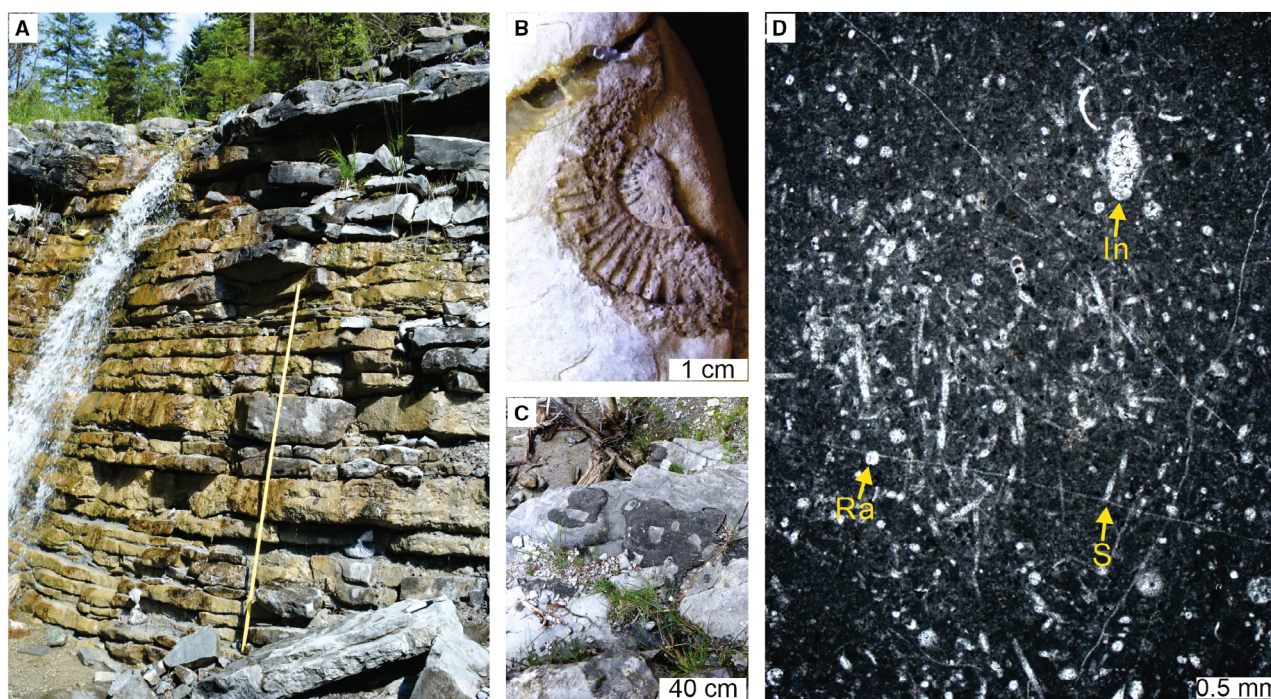


**Fig. 16.** (A) Scheibelberg Formation, comprising grey bedded limestones with chert nodules and containing abundant fossils, the Lahnewies Syncline section (Nudelgraben Creek part). (B) Ammonoid *Schlotheimia* sp., representing a late Hettangian age. (C) Chert nodules. (D) Abundant siliceous sponge spicules (S), radiolarians (Ra) and foraminifera, for example, *Involutina* sp. (IN) are observed. Yellow stick = 2 m.

organic matter, samples from the Lahnewies Syncline section were subsequently analysed for lipid biomarkers.

### Primary producers through the P–T and T–J critical intervals

In the P–T boundary section in Xiakou, masses of calcispheres occur in one distinct carbonate layer P<sub>15-2</sub> (MF-5) that is interlayered between volcanic ash interlayers (layers P<sub>15-1</sub> and P<sub>15-3</sub>) and characterized by peloidal textures (Fig. 6A and B). In the T–J boundary section, calcispheres are also quite abundant. The term ‘calcisphere’ derives from *Calcisphaera*, a genus originally established for specific calcareous microfossils in Carboniferous carbonates (Williamson, 1880), but is nowadays commonly used for spherical calcareous microfossils of various origins.

Calcispheres in Upper Triassic or younger rocks were commonly interpreted as cysts of calcareous dinoflagellates (Keupp, 1991; Wendler & Bown, 2013), perhaps reflecting the onset of significant calcification of pelagic plankton (Corso *et al.*, 2021). The biological affinities of

calcispheres in Middle Triassic and older rocks, in contrast, are disputed. For instance, it has been proposed that some Silurian calcispheres might represent ancestors of dinoflagellates (Servais *et al.*, 2009), whilst specimens from the Late Devonian were interpreted as radiolarians (Antoshkina, 2006). Abundant calcispheres in microbialites at the P–T boundary (e.g. Pei *et al.*, 2019; Zhang *et al.*, 2020) perhaps represented coccoid cyanobacteria (Zhang *et al.*, 2020). In the light of these findings, the biological affinity of calcispheres in layer P<sub>15-2</sub> at Xiakou (Figs 6C to 6F, 7 and 8) remains unclear, although it is tempting to speculate that they represent ancestors of dinoflagellates.

In the T–J boundary section, calcisphere-rich samples have high TOC contents (up to 6.18 wt.%; Table 1) and show a dominance of eukaryotic steranes over bacterial hopanes (ster/hop = 2.7 to 6.0; Table 2), pointing to a eutrophic environment with an algae-dominated primary production (e.g. Love & Zumberge, 2021). This is in good accordance with relatively high amounts of pristane and phytane, which are commonly sourced by phototrophic primary producers (e.g. Peters *et al.*, 2005).

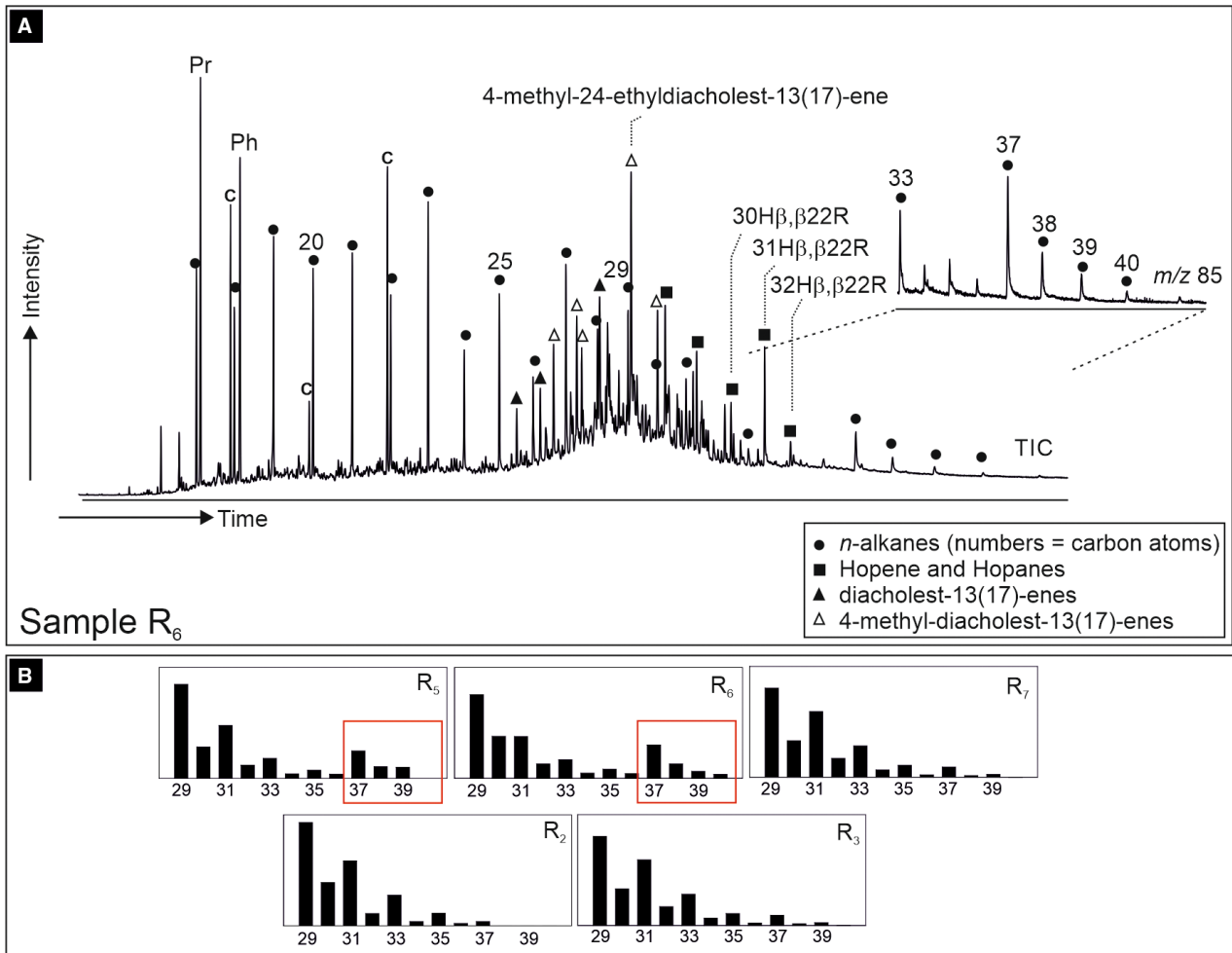


**Fig. 17.** (A) Exemplified total ion chromatogram of the aliphatic fraction of sample R<sub>6</sub> in the top layer of the T-Bed, the Lahnewies Syncline section (Lahnewies Creek part) with *m/z* 85 ion chromatogram. Diacholest-13(17) enes and 4-methyl diacholest-13(17)-enes are the most abundant among steroids. Note that the major compound, which is tentatively identified as (20R-10 $\alpha$ )-4-methyl-24-ethyldiacholest-13(17)-ene could also be 4-methyl-23,24-dimethyldiacholest-13(17)-ene (e.g. Volkman *et al.*, 2015). Pr, pristane; Ph, phytane; c, laboratory contaminants, for example, 30H $\beta$ , $\beta$ 22R = 17 $\beta$ (H),21 $\beta$ (H)-22R-hopane (C<sub>30</sub>). (B) Relative abundances of individual *n*-alkanes from *m/z* 85 ion chromatograms, demonstrating the uncommon prevalence of *n*-C<sub>37</sub>, *n*-C<sub>38</sub> and *n*-C<sub>39</sub> *n*-alkanes particularly in samples R<sub>5</sub> and R<sub>6</sub>.

**Table 2.** Selected biomarker ratios, including the Carbon Preference Index  $CPI = 0.5 \times ((n-C_{25} + n-C_{27} + n-C_{29} + n-C_{31}) / (n-C_{26} + n-C_{28} + n-C_{30} + n-C_{32}) + (n-C_{25} + n-C_{27} + n-C_{29} + n-C_{31}) / (n-C_{24} + n-C_{26} + n-C_{28} + n-C_{30}))$ , pristane/phytane (Pr/Ph), calculated from flame ionization detector (FID) responses, and steranes/hopanes (Ster/Hop), dinosteranes/(steranes + dinosteranes), from multiple-reaction monitoring (MRM) analyses. R, Rhaetian.

Section	Sample	CPI	Pr/Ph	Ster/Hop	Dinosteranes/(steranes + dinosteranes)
Lahnewies-Syncline	R <sub>2</sub>	1.7	1.3	3.2	0.04
	R <sub>3</sub>	1.8	0.9	6.0	0.05
	R <sub>5</sub>	2.7	1.0	3.8	0.33
	R <sub>6</sub>	1.7	1.2	2.7	0.11
	R <sub>7</sub>	2.7	1.2	3.2	0.21

However, parts of those compounds may also derive from higher land plants, as indicated by a prevalence of odd-numbered hydrocarbons between  $n$ -C<sub>24</sub> and  $n$ -C<sub>32</sub> (CPIs = 1.7 to 2.7) (Table 2; Fig. 17A; Eglinton *et al.*, 1962).

Remarkably,  $n$ -alkanes in samples from the T–J boundary section commonly show a marked increase in abundance between C<sub>37</sub> and C<sub>39</sub>, particularly in samples R<sub>5</sub> and R<sub>6</sub> (Fig. 17B). This distinct feature requires explanation as the relative abundance of  $n$ -alkanes  $>n$ -C<sub>33</sub> usually drops with increasing carbon number.  $N$ -alkanes with carbon numbers between 37 and 39 might derive from long-chain alkenones, which are ubiquitous in recent haptophytes (Cranwell, 1985; Brassell *et al.*, 1986; Prahl *et al.*, 1988). Haptophytes became abundant in the Triassic (De Vargas *et al.*, 2007), but to the best of present knowledge alkenones have not been found in rocks older than the Jurassic (Dumitrescu & Brassell, 2003). However, it was experimentally demonstrated that the mild reduction of alkenones, as to be expected during diagenesis, results in the formation of  $n$ -alkanes with identical chain lengths (Love *et al.*, 2005), supporting a precursor–product relationship between these compounds. It thus appears plausible that the observed  $n$ -C<sub>37–39</sub> alkanes are diagenetic derivatives of alkenones that originated from early haptophytes such as coccolithophorids.

Notably, samples from the T–J boundary section also contained dinosteranes and 4-methyl-24-ethylcholestene (or possibly a dinosterane-derived 4,23,24-trimethylcholestene) (Fig. 17A), which both could be sourced by dinoflagellates (Summons *et al.*, 1987). This is in good agreement with findings from Late Triassic rocks in the Bristol Trough (UK) that also contained abundant dinosteranes and other 4-methyl steranes (Thomas *et al.*, 1993). 4-methyl steranes can also derive from methanotrophic bacteria, but typically lack an alkylation at C-24 (e.g. Bird *et al.*, 1971; Jahnke, 1992; Volkman *et al.*, 2015), resulting in different mass spectra (Birgel & Peckmann, 2008). 4-methyl-24-ethylcholestene has previously been reported from recent haptophyte algae of the order Pavloales (Volkman *et al.*, 1990, 1997), sometimes co-occurring with alkenones (Schöner, 2001). Together with the prominent C<sub>37–39</sub>  $n$ -alkanes, dinosteranes and 4-methyl-24-ethylcholestene indicate major contributions by dinoflagellates and haptophytes to the organic matter in the T–J boundary section.

### Ecosystem changes through the P–T and T–J critical intervals – Is volcanism the common driver?

The P–T and T–J crises both have been intimately associated with large continental flood basalt provinces (i.e. the Siberian Traps and CAMP, respectively) (e.g. Whiteside *et al.*, 2010; Blackburn *et al.*, 2013; Burgess & Bowring, 2015; Thibodeau *et al.*, 2016; Burgess *et al.*, 2017; Davies *et al.*, 2017; Percival *et al.*, 2017; Broadley *et al.*, 2018; Wang *et al.*, 2018). The Siberian Traps are one of the largest known continental flood basalt provinces of the Phanerozoic, with an estimated original volume of  $ca\ 3 \times 10^6\ km^3$  (Reichow *et al.*, 2002). About two-thirds of the total lava/pyroclastic volume erupted over a period of only  $ca\ 300\ 000$  years, shortly before and concurrent with the end-Permian mass extinction (Burgess & Bowring, 2015), and concurrent with a massive emplacement of sill intrusions (Burgess *et al.*, 2017). Simultaneously, the volcanism liberated significant amounts of volatiles such as halogens, carbon dioxide, sulphur dioxide and methane (Svensen *et al.*, 2009; Ogden & Sleep, 2012; Broadley *et al.*, 2018; Clapham & Renne, 2019), perhaps resulting in a six-fold increase of atmospheric  $pCO_2$  during this crisis (Wu *et al.*, 2021).

Negative excursions of both  $\delta^{44/40}Ca$  (in carbonates and hydroxyapatites) and  $\delta^{13}C$  (in carbonates and organic matter) indicated that the elevated  $pCO_2$  levels may have caused ocean acidification (Payne *et al.*, 2010; Hinojosa *et al.*, 2012; Silva-Tamayo *et al.*, 2018). Indeed, shallow marine successions from that time commonly exhibit an erosional surface between latest Permian carbonates and post-extinction microbialites, perhaps reflecting a decreased seawater pH (Payne *et al.*, 2007; Collin *et al.*, 2009; Lehrmann *et al.*, 2015; Pei *et al.*, 2019). Acidification, together with physiological effects such as hypercapnia, seems to be consistent with the selective extinction of organisms with calcareous shells and poorly buffered respiratory physiology (Knoll *et al.*, 2007; Clapham & Payne, 2011; for an alternative view see Slater *et al.*, 2022).

At Xiakou, the calcisphere-rich layer P<sub>15-2</sub> (MF-5) is intercalated in volcanic ash (layers P<sub>15-1</sub> and P<sub>15-3</sub>) (Fig. 2), perhaps indicating a direct relationship between volcanism and planktonic primary production. One plausible explanation is that high nutrition associated with volcanism resulted in a fertilization of

marine environments, thereby promoting primary production in the ecosystems. This hypothesis is supported by studies that demonstrated a positive impact of volcanic eruptions on primary production in modern marine environments such as the Korean coast and the western Pacific Ocean (Zhang *et al.*, 2017; Kim, 2020).

Like the Siberian Traps, CAMP classifies as one of the largest known Phanerozoic continental flood basalt provinces (Kravchinsky, 2012). The formation of the CAMP and large-scale intrusive processes are synchronous to the T–J extinction event, possibly implying a direct connection (Blackburn *et al.*, 2013; Davies *et al.*, 2017). Marine sedimentary successions show negative  $\delta^{13}\text{C}_{\text{carb}}$  and  $\delta^{13}\text{C}_{\text{org}}$  excursions at the time of CAMP (Ruhl *et al.*, 2010, 2011; Whiteside *et al.*, 2010; Ruhl & Kürschner, 2011; Corso *et al.*, 2014). Furthermore, a biocalcification crisis occurred during this time, which was likely linked to ocean water acidification because organisms with aragonitic or high-Mg calcite skeletons and a weak physiological control on biomineralization were particularly affected (Hautmann *et al.*, 2008; Ruhl *et al.*, 2010).

The T–J Lahnewies Syncline section records three regionally widespread anoxic events. The first two events are characterized by mass extinctions of certain ammonoids, as expressed in the names of respective beds (*Choristoceras* Bed and *Epsilonoceras* Bed) (Fig. 4; Reitner, 1978; Karl *et al.*, 2014). The third event is reflected by the top layer of the T-Bed and almost results in a collapse of carbonate production. Palaeontological and organic geochemical data evidence a eutrophic ecosystem dominated by algae such as calcified haptophytes (i.e. coccolithophores) and dinoflagellates during the event (Figs 11C, 11D, 12D to 12M and 17; McRoberts *et al.*, 2012; Hillebrandt *et al.*, 2013). Notably, biomarkers indicative for water column stratification and photic zone anoxia (for example, gammacerane, isorenieratane), as detected in contemporaneous sections from other regions (Richoz *et al.*, 2012; Blumenberg *et al.*, 2016), have not been found.

The Lahnewies Syncline section provides no evidence for a direct influence of CAMP-related volcanic activity on uppermost Rhaetian environments. For instance, clay minerals that are commonly sourced by volcanic eruptions (for example, montmorillonite, bentonite, possibly smectite) have not been observed. The only potential indication is clay spherules contained in the topmost Kössen Formation of the

Kendelbach section, which perhaps represents altered volcanic ash layers (Zajzon *et al.*, 2012). However, CAMP might have affected local environments by supplying high quantities of fertilizing volatiles, carbon dioxide and sulphur dioxide to the atmosphere, resulting in acidic rain, and leading to ocean eutrophication (Davies *et al.*, 2017). Thus, a possible relationship between volcanism and abundant dinoflagellates and coccolithophorids in the top layer of the T-Bed is plausible and requires further investigation (Figs 11C, 11D, 12D to 12M and 17).

## CONCLUSIONS

This study focuses on ecological upheavals through the Permian–Triassic (P–T) and Triassic–Jurassic (T–J) critical intervals, which are commonly assumed to be caused by voluminous volcanic provinces [Siberian Traps and Central Atlantic Magmatic Province (CAMP), respectively]. Calcispheres, interpreted as dinoflagellates and/or coccolithophorids, are abundant in deposits from both intervals. Additionally, the T–J section preserves abundant 4-methyl steranes (diagnostic for dinoflagellates) and  $\text{C}_{37-39}$  *n*-alkanes (indicative for haptophytes). In the P–T boundary section from South China, calcispheres occur in a distinct limestone bed that is intercalated in thick volcanic ash beds, which is probably related to the Siberian Traps. Thus, volcanism might have had a positive effect on the planktonic primary producers, perhaps by delivering essential nutrients. The studied T–J boundary sections from Northern Calcareous Alps, in contrast, preserve no sedimentological evidence for volcanic activity. Thus, a possible relationship between volcanism and blooms of dinoflagellates and coccolithophorids remains elusive and needs further investigation.

## ACKNOWLEDGEMENTS

We thank N. Sheldon, P. Suarez-Gonzalez and an anonymous reviewer for valuable comments and suggestions. Many thanks are given to A. Munnecke, A.L. Claußen, E. Jarochowska, G. Mathes, L.M. Baumann, M. Natalicchio, P. Suarez-Gonzalez and S. Kiel for helpful discussions. B. Feng, D. Grabow, E. Siedersbeck, G. Wu, H. Mei, Y. He and Z-Q. Chen are thanked for field assistance. A. Freiberg, A. Hackmann, A. Pack, A. Reimer, B. Röring, C. Conradt, D.



Hause-Reitner, D. Kohl, G. Scheeder, J. Dyckmans, J. Schönig, K. Lünsdorf, K. Wemmer, P. Adam, T. Wasselin and W. Dröse are acknowledged for lab. assistance. This study was financially supported by the China Council Scholarship (CSC) and a Teach@Tübingen Fellowship by the University of Tübingen (Germany). The Forestry Department Oberammergau (Bayerische Staatsforsten) gave permission to drive on closed forest roads. Open Access funding enabled and organized by Projekt DEAL.

## REFERENCES

- Aloy, J., Aberhan, M., Bottjer, D.J., Foote, M., Fürsich, F.T., Harries, P.J., Hendy, A.J.W., Holland, S.M., Ivany, L.C., Kiessling, W., Kosnik, M.A., Marshall, C.R., McGowan, A.J., Miller, A.I., Olszewski, T.D., Patzkowsky, M.E., Peters, S.E., Villier, L., Wagner, P.J., Bonuso, N., Borkow, P.S., Brenneis, B., Clapham, M.E., Fall, L.M., Ferguson, C.A., Hanson, V.L., Krug, A.Z., Layou, K.M., Leckey, E.H., Nürnberg, S., Powers, C.M., Sessa, J.A., Simpson, C., Tomašových, A. and Visaggi, C.C. (2008) Phanerozoic trends in the global diversity of marine invertebrates. *Science*, **321**, 97–100.
- Antoshkina, A.I. (2006) Palaeoenvironmental implications of Palaeomicrocodium in upper Devonian microbial mounds of the Chernyshev swell, Timan-northern Ural region. *Facies*, **52**, 611–625.
- Bambach, R.K. (2006) Phanerozoic biodiversity mass extinctions. *Annual Rev. Earth Planet. Sci.*, **34**, 127–155.
- Bernasconi, S.M., Meier, I., Wohlwend, S., Brack, P., Hochuli, P.A., Bläsi, H., Wortmann, U.G. and Ramseyer, K. (2017) An evaporite-based high-resolution sulfur isotope record of late Permian and Triassic seawater sulfate. *Geochim. Cosmochim. Acta*, **204**, 331–349.
- Bernecker, M., Weidlich, O. and Flügel, E. (1999) Response of Triassic reef coral communities to sea-level fluctuations, storms and sedimentation: evidence from a spectacular outcrop (Adnet, Austria). *Facies*, **40**, 229–279.
- Bird, C.W., Lynch, J.M., Pirt, S.J., Reid, W.W., Brooks, C.J.W. and Middleditch, B.S. (1971) Steroids and squalene in *Methylococcus capsulatus* grown on methane. *Nature*, **230**, 473–474.
- Birgel, D. and Peckmann, J. (2008) Aerobic methanotrophy at marine methane seeps: A synthesis. *Org. Geochem.*, **59**, 1659–1667.
- Blackburn, T.J., Olsen, P.E., Bowring, S.A., McLean, N.M., Kent, D.V., Puffer, J., McHone, G., Rasbury, E.T. and Et-Touhami, M. (2013) Zircon U-Pb geochronology links the end-Triassic extinction with the Central Atlantic Magmatic Province. *Science*, **340**, 941–945.
- Blumenberg, M., Heunisch, C., Lückge, A., Scheeder, G. and Wiese, F. (2016) Photic zone euxinia in the central Rhaetian Sea prior the Triassic-Jurassic boundary. *Palaeogeogr. Palaeoclimatol., Palaeoecol.*, **461**, 55–64.
- Blumenberg, M., Zink, K.G., Scheeder, G., Ostertag-Henning, C. and Erbacher, J. (2019) Biomarker palaeoreconstruction of the German Wealden (Berriasian, early cretaceous) in the Lower Saxony Basin (LSB). *Int. J. Earth Sci.*, **108**, 229–244.
- Böhm, F. (2003) Lithostratigraphy of the Adnet group (lower to middle Jurassic, Salzburg, Austria). In: *Stratigraphia Austriaca: Österreichischen Akademie der Wissenschaften, Schriftenreihe der Erdwissenschaftlichen Kommission* (Ed. Piller, W.E.), Vol. **16**, pp. 231–268. Austrian Academy of Sciences, Vienna, Austria.
- Bown, P.R. (1987a) The structural development of early Mesozoic coccoliths and its evolutionary and taxonomic significance. *Abhandlungen der Geologischen Bundesanstalt*, **39**, 33–49.
- Bown, P.R. (1987b) Taxonomy, evolution, and biostratigraphy of late Triassic-early Jurassic calcareous nannofossils. *Spec. Pap. Palaeontol.*, **38**, 1–118.
- Bown, P.R., Lees, J.A. and Young, J.R. (2004) Calcareous nannoplankton evolution and diversity through time. In: *Coccolithophores: From Molecular Processes to Global Impact* (Eds Thierstein, H.R. and Young, J.R.), pp. 481–508. Springer-Verlag, Berlin, Heidelberg.
- Brassell, S.C., Eglinton, G., Marlowe, I.T., Pflaumann, U. and Sarnthein, M. (1986) Molecular stratigraphy: a new tool for climatic assessment. *Nature*, **320**, 129–133.
- Brennecke, G.A., Herrmann, A.D., Algeo, T.J. and Anbar, A.D. (2011) Rapid expansion of oceanic anoxia immediately before the end-Permian mass extinction. *Proc. Natl. Acad. Sci.*, **108**, 17631–17634.
- Broadley, M.W., Barry, P.H., Ballentine, C.J., Taylor, L.A. and Burgess, R. (2018) End-Permian extinction amplified by plume-induced release of recycled lithospheric volatiles. *Nat. Geosci.*, **11**, 682–687.
- Burgess, S.D. and Bowring, S.A. (2015) High-precision geochronology confirms voluminous magmatism before, during, and after Earth's most severe extinction. *Sci. Adv.*, **1**, e1500470.
- Burgess, S.D., Muirhead, J.D. and Bowring, S.A. (2017) Initial pulse of Siberian traps sills as the trigger of the end-Permian mass extinction. *Nat. Commun.*, **8**, 164.
- Clapham, M.E. and Payne, J.L. (2011) Acidification, anoxia, and extinction: A multiple logistic regression analysis of extinction selectivity during the middle and late Permian. *Geology*, **39**, 1059–1062.
- Clapham, M.E. and Renne, P.R. (2019) Flood basalts and mass extinctions. *Annu. Rev. Earth Planet. Sci.*, **47**, 275–303.
- Clarkson, M.O., Kasemann, S.A., Wood, R.A., Lenton, T.M., Daines, S.J., Richoz, S., Ohnemüller, F., Meixner, A., Poulton, S.W. and Tipper, E.T. (2015) Ocean acidification and the Permo-Triassic mass extinction. *Science*, **348**, 229–232.
- Collin, P.-Y., Kershaw, S., Crasquin-Soleau, S. and Feng, Q. (2009) Facies changes and diagenetic processes across the Permian-Triassic boundary event horizon, great Bank of Guizhou, South China: a controversy of erosion and dissolution. *Sedimentology*, **56**, 677–693.
- Corso, J.D., Marzoli, A., Tateo, F., Jenkyns, H.C., Bertrand, H., Youbi, N., Mahmoudi, A., Font, E., Buratti, N. and Cirilli, S. (2014) The dawn of CAMP volcanism and its bearing on the end-Triassic carbon cycle disruption. *J. Geol. Soc. London*, **171**, 153–164.
- Corso, J.D., Preto, N., Agnini, C., Hohn, S., Merico, A., Willems, H. and Gianolla, P. (2021) Rise of calcispheres during the Carnian pluvial episode (late Triassic). *Global Planet. Change*, **200**, 103453.
- Cranwell, P.A. (1985) Long-chain unsaturated ketones in recent lacustrine sediments. *Geochim. Cosmochim. Acta*, **49**, 1545–1551.

- Davies, J.H.F.L., Marzoli, A., Bertrand, H., Youbi, N., Ernesto, M. and Schaltegger, U. (2017) End-Triassic mass extinction started by intrusive CAMP activity. *Nat. Commun.*, **8**, 15596.
- De Vargas, C., Aubry, M.-P., Probert, I.A.N. and Young, J. (2007) CHAPTER 12 - origin and evolution of coccolithophores: from coastal hunters to oceanic farmers. In: *Evolution of Primary Producers in the Sea* (Eds Falkowski, P.G. and Knoll, A.H.), pp. 251–285. Academic Press, Burlington, NJ.
- Demangel, I., Kovács, Z., Richoz, S., Gardin, S., Krystyn, L., Baldermann, A. and Piller, W.E. (2020) Development of early calcareous nannoplankton in the late Triassic (northern calcareous Alps, Austria). *Global Planet. Change*, **193**, 103254.
- Dumitrescu, M. and Brassell, S.C. (2003) Biomarkers confirm cyanobacteria as a major source of planktonic organic matter during the early Aptian. *GSA 2003 Annual Meeting, Seattle*.
- Eglinton, G., Hamilton, R.J., Raphael, R.A. and Gonzales, A.G. (1962) Hydrocarbon constituents of the wax coatings of plant leaves: A taxonomic study. *Nature*, **193**, 739–742.
- Espitalié, J., Laporte, J.L., Madec, M., Marquis, F., Leplat, P., Paulet, J. and Boutefeu, A. (1977) Méthode rapide de caractérisation des roches mères, de leur potentiel pétrolier et de leur degré d'évolution. *Revue de l'Institut Français du Pétrole*, **32**, 23–42.
- Fabricius, F.H. (1966) Beckensedimentation und Riffbildung an der Wende Trias/Jura in den Bayerisch-Tiroler Kalkalpen. *Int. Sediment. Petrograp. Ser. Brill Leiden*, **9**, 1–143.
- Fan, J.-X., Shen, S.-Z., Erwin, D.H., Sadler, P.M., MacLeod, N., Cheng, Q.-M., Hou, X.-D., Yang, J., Wang, X.-D., Wang, Y., Zhang, H., Chen, X., Li, G.-X., Zhang, Y.-C., Shi, Y.-K., Yuan, D.-X., Chen, Q., Zhang, L.-N., Li, C. and Zhao, Y.-Y. (2020) A high-resolution summary of Cambrian to early Triassic marine invertebrate biodiversity. *Science*, **367**, 272–277.
- Feng, Z., Yang, Y. and Jin, Z. (1997) *Lithofacies Paleogeography of Permian of South China*. China University of Petroleum Press, Beijing.
- Galbrun, B., Boulila, S., Krystyn, L., Richoz, S., Gardin, S., Bartolini, A. and Maslo, M. (2020) “Short” or “long” Rhaetian? Astronomical calibration of Austrian key sections. *Global Planet. Change*, **192**, 103253.
- Gao, Q., Zhang, N., Xia, W., Feng, Q., Chen, Z.-Q., Zheng, J., Griffin, W.L., O'Reilly, S.Y., Pearson, N.J., Wang, G., Wu, S., Zhong, W. and Sun, X. (2013) Origin of volcanic ash beds across the Permian–Triassic boundary, Daxiakou, South China: Petrology and U–Pb age, trace elements and Hf-isotope composition of zircon. *Chem. Geol.*, **360–361**, 41–53.
- Greene, S.E., Bottjer, D.J., Corsetti, F.A., Berelson, W.M. and Zonneveld, J.-P. (2012) A seafloor carbonate factory across the Triassic–Jurassic transition. *Geology*, **40**, 1043–1046.
- Gümbel, C.W. (1861) *Geognostische Beschreibung des bayerischen Alpengebirges und seines Vorlandes*. Verlag von Justus Perthes, Gotha.
- Hautmann, M., Benton, M.J. and Tomašových, A. (2008) Catastrophic Ocean acidification at the Triassic–Jurassic boundary. *Neues Jahrbuch für Geologie und Paläontologie, Abh.*, **249**, 119–127.
- Hillebrandt, A.V. and Krystyn, L. (2009) On the oldest Jurassic ammonites of Europe (northern calcareous Alps, Austria) and their global significance. *Neues Jahrbuch für Mineralogie, Geologie und Paläontologie*, **253**, 163–195.
- Hillebrandt, A.V., Krystyn, L. and Kürschner, W.M. (2007) A candidate GSSP for the base of the Jurassic in the northern calcareous Alps (Kuhjoch section, Karwendel Mountains, Tyrol, Austria). *Int. School Jain Stud. Newslett.*, **34**, 2–20.
- Hillebrandt, A.V., Krystyn, L., Kürschner, W.M., Bonis, N.R., Ruhl, M., Richoz, S., Schobben, M.A.N., Urlichs, M., Bown, P.R., Kment, K., McRoberts, C.A., Simms, M. and Tomášových, A. (2013) The global Stratotype sections and point (GSSP) for the base of the Jurassic system at Kuhjoch (Karwendel Mountains, northern calcareous Alps, Tyrol, Austria). *Episodes*, **36**, 162–198.
- Hinojosa, J.L., Brown, S.T., Chen, J., DePaolo, D.J., Paytan, A., Shen, S.-Z. and Payne, J.L. (2012) Evidence for end-Permian Ocean acidification from calcium isotopes in biogenic apatite. *Geology*, **40**, 743–746.
- Hong, H., Xie, S. and Lai, X. (2011) Volcanism in association with the prelude to mass extinction and environment change across the Permian–Triassic boundary (PTB), southern China. *Clays Clay Min.*, **59**, 478–489.
- Hornung, T. and Haas, U. (2017) *Geologische Karte von Bayern 1:25.000, Erläuterungen zu den Blättern 8531/8631 Zugspitze and 8532/8632*, pp. 1–151. Bayerisches Landesamt für Umwelt, Garmisch-Partenkirchen.
- Huang, Y., Chen, Z.-Q., Wignall, P.B. and Zhao, L. (2017) Latest Permian to middle Triassic redox condition variations in ramp settings, South China: pyrite framboid evidence. *Geol. Soc. Am. Bull.*, **129**, 229–243.
- Jafar, S.A. (1983) Significance of late Triassic calcareous nannoplankton from Austria and southern Germany. *Neues Jahrbuch für Geologie und Paläontologie – Abhandlungen*, **66**, 218–259.
- Jahnke, L.L. (1992) The effects of growth temperature on the methyl sterol and phospholipid fatty acid composition of *Methylococcus capsulatus* (Bath). *Fed. Eur. Microbiol. Soc. Microbiol. Lett.*, **93**, 209–212.
- Janofske, D. (1987) Kalkige Nannofossilien aus der Ober-Trias (Rhät) der Nördlichen Kalkalpen. *Berliner Geowissenschaftliche Abhandlungen*, **86**, 45–67.
- Janofske, D. (1992) Kalkiges Nannoplankton, insbesondere Kalkige Dinoflagellaten-Zysten der alpinen Ober-Trias: Taxonomie, Biostratigraphie und Bedeutung für die Phylogenie der Peridiniales. *Berliner Geowissenschaftliche Abhandlungen*, **E4**, 1–53.
- Jaraula, C.M.B., Grice, K., Twitchett, R.J., Böttcher, M.E., LeMetayer, P., Dastidar, A.G. and Opazo, L.F. (2013) Elevated  $p\text{CO}_2$  leading to late Triassic extinction, persistent photic zone euxinia, and rising sea levels. *Geology*, **41**, 955–958.
- Joachimski, M.M., Lai, X., Shen, S., Jiang, H., Luo, G., Chen, B., Chen, J. and Sun, Y. (2012) Climate warming in the latest Permian and the Permian–Triassic mass extinction. *Geology*, **40**, 195–198.
- Karl, H.-V., Arp, G., Siedersbeck, E. and Reitner, J. (2014) A large ichthyosaur vertebra from the lower Kösse formation (upper Norian) of the Lahnewiesgraben near Garmisch-Partenkirchen, Germany. *Göttingen Contrib. Geosci.*, **77**, 191–197.
- Keupp, H. (1991) Fossil calcareous dinoflagellate cysts. In: *Calcareous Algae and Stromatolites* (Ed. Riding, R.), pp. 267–286. Springer-Verlag, Berlin, Heidelberg.
- Kim, T.-J. (2020) Harmful algal blooms associated with volcanic eruptions in Indonesia and Philippines for

- Korean fishery damage. *Adv. Biosci. Biotechnol.*, **11**, 217–236.
- Kment, K.** (2000) Frühe liassische Ammoniten aus der Gegend um Hinterriß im Karwendelgebirge (Tirol) und dem Mangfallgebirge bei Rottach-Egern (Bayern). *Jahrbuch der Geologischen Bundesanstalt*, **142**, 181–218.
- Knoll, A.H., Bambach, R.K., Payne, J.L., Pruss, S. and Fischer, W.W.** (2007) Paleophysiology and end-Permian mass extinction. *Earth Planet. Sci. Lett.*, **256**, 295–313.
- Kozur, H. and Mock, R.** (1991) New middle Carnian and Rhaetian conodonts from Hungary and the Alps. Stratigraphic importance and tectonic implications for the Buda Mountains and adjacent areas. *Jahrbuch der Geologischen Bundesanstalt*, **134**, 271–297.
- Kravchinsky, V.A.** (2012) Paleozoic large igneous provinces of northern Eurasia: correlation with mass extinction events. *Global Planet. Change*, **86–87**, 31–36.
- Krystyn, L.** (1987) Zur Rhät-Stratigraphie in den Zlambach-Schichten (vorläufiger Bericht). *Sitzungsberichte der Akademie der Wissenschaften Mathematisch-Naturwissenschaftliche Klasse*, **196**, 21–36.
- Krystyn, L.** (2008) An ammonoid-calibrated Tethyan conodont time scale of the late upper Triassic. *Berichte der Geologischen Bundesanstalt*, **76**, 9–11.
- Krystyn, L., Böhm, F., Kürschner, W.M. and Delecat, S.** (2005) The Triassic Jurassic boundary in the northern calcareous Alps. In: *Triassic-Jurassic Boundary Events: 5th Field Workshop, IGCP 458 Project* (Eds Palfy, J. and Oszvart, P.), pp. A1–A39. Tata, Hallein.
- Kuhnert, C.** (1967) *Erläuterungen zur geologischen Karte von Bayern 1:25.000. Blatt Nr. 8432 Oberammergau.* Bayerisches Geologisches Landesamt, München.
- Kuss, J.** (1983) Faziesentwicklung in proximalen Intraplattform Becken: Sedimentation, Palökologie und Geochemie der Kössener Schichten (Ober-Trias, Nördliche Kalkalpen). *Facies*, **9**, 61–171.
- Lafargue, E., Marquis, F. and Pillot, D.** (1998) Rock-Eval 6 applications in hydrocarbon exploration, production, and soil contamination studies. *Revue de l'Institut français du pétrole*, **53**, 421–437.
- Langel, R. and Dyckmans, J.** (2014) Combined  $^{13}\text{C}$  and  $^{15}\text{N}$  isotope analysis on small samples using a near-conventional elemental analyzer/isotope ratio mass spectrometer setup. *Rapid Commun. Mass Spectrom.*, **28**, 1019–1022.
- Langel, R. and Dyckmans, J.** (2017) A closer look into the nitrogen blank in elemental analyser/isotope ratio mass spectrometry measurements. *Rapid Commun. Mass Spectrom.*, **31**, 2051–2055.
- Lehrmann, D.J., Bentz, J.M., Wood, T., Goers, A., Dhillon, R., Akin, S., Li, X., Payne, J.L., Kelley, B.M., Meyer, K.M., Schaal, E.K., Suarez, M.B., Yu, M., Qin, Y., Li, R., Minzoni, M. and Henderson, C.M.** (2015) Environmental controls on the genesis of marine microbialites and dissolution surface associated with the end-Permian mass extinction: new sections and observations from the Nanpanjiang Basin, South China. *Palaio*, **30**, 529–552.
- Love, G.D. and Zumberge, J.A.** (2021) *Emerging Patterns in Proterozoic Lipid Biomarker Records (Elements in Geochemical Tracers in Earth System Science).* Cambridge University Press, Cambridge.
- Love, G.D., Bowden, S.A., Jahnke, L.L., Snape, C.E., Campbell, C.N., Day, J.G. and Summons, R.E.** (2005) A catalytic hydrolysis method for the rapid screening of microbial cultures for lipid biomarkers. *Org. Geochem.*, **36**, 63–82.
- Luo, J., He, Y., Wang, D., Zhou, X., Tian, Y., Liu, N. and Li, H.** (2009) Petrological characteristics and sedimentary environment analysis of the Permian of Daxiakou section, Kingshan County, Hubei Province. *J. Palaeogeogr.*, **11**, 393–404 (in Chinese).
- Luo, G., Kump, L.R., Wang, Y., Tong, J., Arthur, M.A., Yang, H., Huang, J., Yin, H. and Xie, S.** (2010) Isotopic evidence for an anomalously low oceanic sulfate concentration following end-Permian mass extinction. *Earth Planet. Sci. Lett.*, **300**, 101–111.
- Mandl, G.W.** (2000) The alpine sector of the Tethyan shelf - examples of Triassic to Jurassic sedimentation and deformation from the northern calcareous Alps. *Mitteilungen der Österreichischen Geologischen Gesellschaft*, **92**, 61–77.
- McRoberts, C.A., Krystyn, L. and Shea, A.** (2008) Rhaetian (late Triassic) *Monotis* (Bivalvia: Pectinoida) from the eastern northern calcareous Alps (Austria) and the end-Norian crisis in pelagic faunas. *Palaentology*, **51**, 721–735.
- McRoberts, C.A., Krystyn, L. and Hautmann, M.** (2012) Macrofaunal response to the end-Triassic mass extinction in the West-Tethyan Kössen Basin, Austria. *Palaio*, **27**, 607–616.
- Mißbach, H., Duda, J.-P., Lünsdorf, N.K., Schmidt, B.C. and Thiel, V.** (2016) Testing the preservation of biomarkers during experimental maturation of an immature kerogen. *Int. J. Astrobiol.*, **15**, 165–175.
- Ogden, D.E. and Sleep, N.H.** (2012) Explosive eruption of coal and basalt and the end-Permian mass extinction. *Proc. Natl. Acad. Sci.*, **109**, 59–62.
- Payne, J.L., Lehrmann, D.J., Wei, J., Orchard, M.J., Schrag, D.P. and Knoll, A.H.** (2004) Large perturbations of the carbon cycle during recovery from the end-Permian extinction. *Science*, **305**, 506–509.
- Payne, J.L., Lehrmann, D.J., Follett, D., Seibel, M., Kump, L.R., Riccardi, A., Altiner, D., Sano, H. and Wei, J.** (2007) Erosional truncation of uppermost Permian shallow-marine carbonates and implications for Permian-Triassic boundary events. *Geol. Soc. Am. Bull.*, **119**, 771–784.
- Payne, J.L., Turchyn, A.V., Paytan, A., DePaolo, D.J., Lehrmann, D.J., Yu, M. and Wei, J.** (2010) Calcium isotope constraints on the end-Permian mass extinction. *Proc. Natl. Acad. Sci.*, **107**, 8543–8548.
- Pei, Y.** (2022) *A Geobiological Approach to Carbonate Factories and Ecosystem Changes Across the Permian-Triassic Boundary.* PhD Thesis. Georg-August-Universität Göttingen, Göttingen.
- Pei, Y., Chen, Z.-Q., Fang, Y., Kershaw, S., Wu, S. and Luo, M.** (2019) Volcanism, redox conditions, and microbialite growth linked with the end-Permian mass extinction: evidence from the Xiajiacao section (western Hubei Province), South China. *Palaeogeogr. Palaeoclimatol. Palaeoecol.*, **519**, 194–208.
- Pei, Y., Duda, J.-P. and Reitner, J.** (2021) Sedimentary factories and ecosystem change across the Permian-Triassic critical interval (P-TrCI): insights from the Xiakou area (South China). *Paläontologische Zeitschrift*, **95**, 709–725.
- Penn, J.L., Deutsch, C., Payne, J.L. and Sperling, E.A.** (2018) Temperature-dependent hypoxia explains biogeography and severity of end-Permian marine mass extinction. *Science*, **362**, 1130.

- Percival, L.M.E., Ruhl, M., Hesselbo, S.P., Jenkyns, H.C., Mather, T.A. and Whiteside, J.H. (2017) Mercury evidence for pulsed volcanism during the end-Triassic mass extinction. *Proc. Natl. Acad. Sci.*, **114**, 7929–7934.
- Peters, K.E. (1986) Guidelines for evaluating petroleum source rock using programmed pyrolysis. *Am. Assoc. Petrol. Geol. Bull.*, **70**, 318–329.
- Peters, K.E. and Cassa, M.R. (1994) Applied source rock geochemistry: chapter 5: part II. Essential elements. In: *The Petroleum System—From Source to Trap* (Eds Peters, K.E., Cassa, M.R., Magoon, L.B. and Dow, W.G.), *American Association of Petroleum Geologists Memoir*, **60**, 93–120.
- Peters, K.E., Walters, C.C. and Moldovan, J.M. (2005) *The Biomarker Guide 2: Biomarkers and Isotopes in Petroleum Systems and Earth History*. Cambridge University Press, Cambridge.
- Petryshyn, V.A., Greene, S.E., Farnsworth, A., Lunt, D.J., Kelley, A., Gammariello, R., Ibarra, Y., Bottjer, D.J., Tripathi, A. and Corsetti, F.A. (2020) The role of temperature in the initiation of the end-Triassic mass extinction. *Earth-Sci. Rev.*, **208**, 103266.
- Prahl, F.G., Muehlhausen, L.A. and Zahnle, D.L. (1988) Further evaluation of long-chain alkenones as indicators of paleoceanographic conditions. *Geochim. Cosmochim. Acta*, **52**, 2303–2310.
- Raup, D.M. (1979) Size of the Permo-Triassic bottleneck and its evolutionary implications. *Science*, **206**, 217–218.
- Raup, D.M. and Sepkoski, J.J. (1982) Mass extinctions in the marine fossil record. *Science*, **215**, 1501–1503.
- Reichow, M.K., Saunders, A.D., White, R.V., Pringle, M.S., Al'Mukhamedov, A.I., Medvedev, A.I. and Kirda, N.P. (2002)  $^{40}\text{Ar}/^{39}\text{Ar}$  dates from the West Siberian Basin: Siberian flood basalt province doubled. *Science*, **296**, 1846–1849.
- Reitner, J. (1978) Ein Teuthiden-Rest aus dem Oberror (Kössener Schichten) der Lahnewies-Neidernachmulde bei Garmisch-Partenkirchen (Bayern). *Paläontologische Zeitschrift*, **52**, 205–212.
- Richo, S., van de Schootbrugge, B., Pross, J., Püttmann, W., Qian, T.M., Lindström, S., Heunisch, C., Fiebig, J., Maquil, R., Schouten, S., Hauzenberger, C.A. and Wignall, P.B. (2012) Hydrogen sulphide poisoning of shallow seas following the end-Triassic extinction. *Nat. Geosci.*, **5**, 662–667.
- Ruhl, M. and Kürschner, W.M. (2011) Multiple phases of carbon cycle disturbance from large igneous province formation at the Triassic-Jurassic transition. *Geology*, **39**, 431–434.
- Ruhl, M., Veld, H. and Kürschner, W.M. (2010) Sedimentary organic matter characterization of the Triassic-Jurassic boundary GSSP at Kuhjoch (Austria). *Earth Planet. Sci. Lett.*, **292**, 17–26.
- Ruhl, M., Bonis, N.R., Reichart, G.-J., Damsté, J.S.S. and Kürschner, W.M. (2011) Atmospheric carbon injection linked to end-Triassic mass extinction. *Science*, **333**, 1043–1046.
- Schäfer, P. (1979) Fazielle Entwicklung und Palökologische Zonierung Zweier Obertriadischer Riffstrukturen in den Nördlichen Kalkalpen (“Oberrhät”-Riff-Kalke, Salzburg). *Facies*, **1**, 3–245.
- Schöner, A.C. (2001) Alkenone in Ostseesedimenten, –schwebstoffen und –algen: Indikatoren für das Paläomilieu? In: *Meereswissenschaftliche Berichte*, Vol. **48**. Institut für Ostseeforschung, Warnemünde.
- Sepkoski, J.J., Bambach, R.K., Raup, D.M. and Valentine, J.W. (1981) Phanerozoic marine diversity and the fossil record. *Nature*, **293**, 435–437.
- Servais, T., Munnecke, A. and Versteegh, G.J.M. (2009) Silurian calcispheres (Calcitarcha) of Gotland (Sweden): comparisons with calcareous dinoflagellates. *Comptes Rendus Palevol*, **8**, 527–534.
- Silva-Tamayo, J.C., Lau, K.V., Jost, A.B., Payne, J.L., Wignall, P.B., Newton, R.J., Eisenhauer, A., Depaolo, D.J., Brown, S., Maher, K., Lehrmann, D.J., Altiner, D., Yu, M., Richoz, S. and Paytan, A. (2018) Global perturbation of the marine calcium cycle during the Permian-Triassic transition. *Geol. Soc. Am. Bull.*, **129**, 229–243.
- Slater, S.M., Bown, P., Twitchett, R.J., Danise, S. and Vajda, V. (2022) Global record of “ghost” nanofossils reveals plankton resilience to high CO<sub>2</sub> and warming. *Science*, **376**, 853–856.
- Song, H., Wignall, P.B., Tong, J. and Yin, H. (2013) Two pulses of extinction during the Permian-Triassic crisis. *Nat. Geosci.*, **6**, 52–56.
- Song, H., Tong, J., Algeo, T.J., Song, H., Qiu, H., Zhu, Y., Tian, L., Bates, S., Lyons, T.W., Luo, G. and Kump, L.R. (2014) Early Triassic seawater sulfate drawdown. *Geochim. Cosmochim. Acta*, **128**, 95–113.
- Stampfli, G.M. and Borel, G.D. (2002) A plate tectonic model for the Paleozoic and Mesozoic constrained by dynamic plate boundaries and restored synthetic oceanic isochrones. *Earth Planet. Sci. Lett.*, **196**, 17–33.
- Summons, R.E., Volkman, J.K. and Boreham, C.J. (1987) Dinosterane and other steroidal hydrocarbons of dinoflagellate origin in sediments and petroleum. *Geochimica et Cosmochimica Acta*, **51**, 3075–3082.
- Sun, Y., Joachimski, M.M., Wignall, P.B., Yan, C., Chen, Y., Jiang, H., Wang, L. and Lai, X. (2012) Lethally hot temperatures during the early Triassic greenhouse. *Science*, **338**, 366–370.
- Svensen, H., Planke, S., Polozov, A.G., Schmidbauer, N., Corfu, F., Podladchikov, Y.Y. and Jamtveit, B. (2009) Siberian gas venting and the end-Permian environmental crisis. *Earth Planet. Sci. Lett.*, **277**, 490–500.
- Sýkora, M., Siblik, M. and Soták, J. (2011) Siliciclastics in the upper Triassic dolomite formations of the Krížna unit (Malá Fatra Mountains, Western Carpathians): constraints for the Carnian pluvial event in the Patric Basin. *Geologica Carpathica*, **62**, 121–138.
- Thibodeau, A.M., Ritterbush, K., Yager, J.A., West, A.J., Ibarra, Y., Bottjer, D.J., Berelson, W.M., Bergquist, B.A. and Corsetti, F.A. (2016) Mercury anomalies and the timing of biotic recovery following the end-Triassic mass extinction. *Nat. Commun.*, **7**, 11147.
- Thomas, J.B., Marshall, J.D., Mann, A.L., Summons, R.E. and Maxwell, J.R. (1993) Dinosteranes (4,23,24-trimethylsteranes) and other biological markers in dinoflagellate-rich marine sediments of Rhaetian age. *Org. Geochem.*, **20**, 91–104.
- Van de Schootbrugge, B. and Wignall, P.B. (2016) A tale of two extinctions: converging end-Permian and end-Triassic scenarios. *Geol. Mag.*, **153**, 332–354.
- Van Krevelen, D.W. (1961) *Coal: Typology-Chemistry-Physics Constitution*. Elsevier, Amsterdam, 514 pp.
- Volkman, J.K., Kearney, P. and Jeffrey, S.W. (1990) A new source of 4-methyl sterols and 5a(H)-stanols in sediments: prymnesiophyte microalgae of the genus pavlova. *Org. Geochem.*, **15**, 489–497.

- Volkman, J.K., Farmen, C.L., Barrett, S.M. and Sikes, E.L. (1997) Unusual dihydroxysterols as chemotaxonomic markers for microalgae from the order Pavlovaales (Haptophyceae). *J. Phycol.*, **33**, 1016–1023.
- Volkman, J.K., Zhang, Z., Xie, X., Qin, J. and Borjigin, T. (2015) Biomarker evidence for Botryococcus and a methane cycle in the Eocene Huadian oil shale, NE China. *Org. Geochem.*, **78**, 121–134.
- Wang, X., Cawood, P.A., Zhao, H., Zhao, L., Grasby, S.E., Chen, Z.-Q., Wignall, P.B., Lv, Z. and Han, C. (2018) Mercury anomalies across the end Permian mass extinction in South China from shallow and deep water depositional environments. *Earth Planet. Sci. Lett.*, **496**, 159–167.
- Wendler, J.E. and Bown, P. (2013) Exceptionally well-preserved cretaceous microfossils reveal new biomineralization styles. *Nat. Commun.*, **4**, 2052.
- Werner, R.A., Bruch, B.A. and Brand, W.A. (1999) ConFlo III – an interface for high precision  $\delta^{13}\text{C}$  and  $\delta^{15}\text{N}$  analysis with an extended dynamic range. *Rapid Commun. Mass Spectrom.*, **13**, 1237–1241.
- Whiteside, J.H., Olsen, P.E., Eglinton, T., Brookfield, M.E. and Sambrotto, R.N. (2010) Compound-specific carbon isotopes from Earth's largest flood basalt eruptions directly linked to the end-Triassic mass extinction. *Proc. Natl. Acad. Sci.*, **107**, 6721–6725.
- Wiedmann, J., Fabricius, F., Krystyn, L., Reitner, J. and Urlichs, M. (1979) Über Umfang und Stellung des Rhaet. *Newslett. Stratigr.*, **8**, 133–152.
- Williamson, W.C. (1880) On the organization of the fossil plants of the coal-measures – part X. including an examination of the supposed radiolarians of the carboniferous rocks. *Philos. Transac. R. Soc. London*, **171**, 493–539.
- Williford, K.H., Foriel, J., Ward, P.D. and Steig, E.J. (2009) Major perturbation in sulfur cycling at the Triassic–Jurassic boundary. *Geology*, **37**, 835–838.
- Wu, Y., Chu, D., Tong, J., Song, H., Corso, J.D., Wignall, P.B., Song, H., Du, Y. and Cui, Y. (2021) Six-fold increase of atmospheric  $p\text{CO}_2$  during the Permian–Triassic mass extinction. *Nat. Commun.*, **12**, 2137.
- Yin, H., Zhang, K., Tong, J., Yang, Z. and Wu, S. (2001) The global Stratotype section and point (GSSP) of the Permian–Triassic boundary. *Episodes*, **24**, 102–114.
- Zajzon, N., Kristály, F., Pálffy, J. and Németh, T. (2012) Detailed clay mineralogy of the Triassic–Jurassic boundary section at Kendlbachgraben (northern calcareous Alps, Austria). *Clay Miner.*, **47**, 177–189.
- Zhang, K.-X., Lai, X.-L., Tong, J.-N. and Jiang, H.-S. (2009) Progresses on study of conodont sequence for the GSSP section at Meishan, Changxing, Zhejiang province, South China. *Acta Palaeontologica Sinica*, **48**, 474–486 (in Chinese).
- Zhang, R., Jiang, T., Tian, Y., Xie, S., Zhou, L., Li, Q. and Jiao, N. (2017) Volcanic ash stimulates growth of marine autotrophic and heterotrophic microorganisms. *Geology*, **45**, 679–682.
- Zhang, F., Algeo, T.J., Romaniello, S.J., Cui, Y., Zhao, L., Chen, Z.-Q. and Anbar, A.D. (2018) Congruent Permian–Triassic  $\delta^{238}\text{U}$  records at Panthalassic and Tethyan sites: confirmation of global-oceanic anoxia and validation of the U-isotope paleoredox proxy. *Geology*, **46**, 327–330.
- Zhang, X.-Y., Zheng, Q.-F., Li, Y., Yang, H.-Q., Zhang, H., Wang, W.-Q. and Shen, S.-Z. (2020) *Polybessurus*-like fossils as key contributors to Permian–Triassic boundary microbialites in South China. *Palaeogeogr. Palaeoclimatol. Palaeoecol.*, **552**, 109770.
- Zhao, L., Chen, Y., Chen, Z.-Q. and Gao, L. (2013) Uppermost Permian to lower Triassic conodont zonation from three gorges area, South China. *Palaaios*, **28**, 523–540.

Manuscript received 19 September 2022; revision accepted 10 January 2023

## Supporting Information

Additional information may be found in the online version of this article:

**Table S1.** X-ray diffraction (XRD) data.